NASA CONTRACTOR REPORT

NASA CR-61224

NASA CR-61224

THE EFFECTS OF SHOCK LAYER RADIATION AND VISCOUS COUPLING ON THE TOTAL HEATING RATE TO A REENTERING BLUNT BODY

Prepared under Contract No. NAS 8-20082 by
L. W. Spradley and C. D. Engel

LOCKHEED MISSILES AND SPACE COMPANY

For

NASA-GEORGE C. MARSHALL SPACE FLIGHT CENTER
Huntsville, Alabama

April 1968

NASA CR-61224

THE EFFECTS OF SHOCK LAYER RADIATION AND VISCOUS COUPLING ON THE TOTAL HEATING RATE TO A REENTERING BLUNT BODY

By

L. W. Spradley and C. D. Engel

Prepared under Contract No. NAS 8-20082 by

LOCKHEED MISSILES AND SPACE COMPANY
Huntsville, Alabama

For

Aero-Astrodynamics Laboratory

NASA-GEORGE C. MARSHALL SPACE FLIGHT CENTER

FOREWORD

This report presents the results of work performed by the Thermal Environment Section of Lockheed's Huntsville Research & Engineering Center. The work was done under subcontract to Northrop Nortronics (NSL PO 5-09287) for Marshall Space Flight Center (MSFC), Contract NAS8-20082. This task was conducted in response to the requirement of Appendix B-1, Schedule Order No. 105.

The NASA Technical Coordinator for this study was Homer Wilson of the Thermal Environment Branch of the Aero-Astrodynamics Laboratory.

SUMMARY

This Technical Memorandum presents some results of a study of coupled convective and radiative heat transfer to vehicles entering planetary atmospheres at superorbital velocities. The flow field about a blunt body in a hypersonic stream is described by a coupled set of conservation equations which are solved numerically using a combination of integral methods and successive approximation techniques. The effects of mass injection, radiative emission and absorption, and coupling between convection and radiation are included in the analysis. The spectral absorption coefficients of the shock layer gas are formulated as functions of temperature, radiation frequency and particle number density. Results obtained for stagnation region convective and radiative heating rates and shock layer profiles are presented for several flight conditions in equilibrium air. Heating rates for a typical lunar type trajectory are also presented. Results of this analysis indicate that the coupling effect of radiation cooling can significantly reduce the total heat transfer to a superorbital entry body.

CONTENTS

Section		Page
	FOREWORD	ii
	SUMMARY	iii
	LIST OF FIGURES	v
	NOMENCLATURE	vii
1	INTRODUCTION	1
2	COUPLED FLOW FIELD ANALYSIS	3
	2.1 Governing Equations	3
	2.2 Method of Solution	7
3	GAS PROPERTIES	11
	3.1 Thermodynamic and Transport Properties	11
	3.2 Radiative Properties	13
4	RESULTS AND DISCUSSION	20
	4.1 Emission and Spectral Absorption Model Results	20
	4.2 Heating Minimization	33
	4.3 Mass Injection Effects	35
	4.4 Earth Entry at Lunar Return Velocities	39
	REFERENCES	42

LIST OF FIGURES

Figure		Page
1	Body-Oriented Coordinate System	4
2	Comparison of Specie Number Density Versus Temperature Calculated Using Two Methods for a Pressure of .68 atm	12
3	Radiative Cross Section of O Atoms as a Function of Frequency for Three Temperatures	15
4	Radiative Cross Section of N Atoms as a Function of Frequency for Three Temperatures	16
5	Radiative Cross Section of N^+ and O^+ as a Function of Frequency for Three Temperatures	17
6	Radiative Cross Section of N_2 and O_2 Molecules as a Function of Frequency	18
7	Shock Layer Pressure and Temperature Profiles	21
8	Radiative Flux Divergence, E, Profiles Obtained from the Spectral and Emission Models	22
9	Absorption Coefficient Versus Frequency for a Typical Wall Condition	24
10	Absorption Coefficient Versus Frequency for Typical Conditions Behind a Shock	25
11	Optical Depth Versus Nondimensional Shock Layer Coordinate for Five Typical Frequencies	26
12	Monochromatic Energy Flux at the Wall Versus Frequency for a Coupled and Uncoupled Solution	27
13	A Comparison of Total Heating Rates Versus Freestream Velocity for Three Freestream Densities (R = 1 ft)	28
14	Shock Layer Temperature and Specie Number Density Profiles for a Flight Condition Producing Strong Radiation Coupling	30

LIST OF FIGURES (Continued)

Figure		Page
15	A Comparison of Total Heating Rates Versus Freestream Velocity for Three Freestream Densities (R = 3 ft)	32
16	Methods Comparison of Heating Rates as a Function of Body Radius	34
17	Heating Rate Parameter Versus Mass Injection Parameter for a Coupled Emission Solution	36
18	Nondimensional Shock Layer Velocity and Enthalpy Profiles for Mass Injection Rates, $(\rho V)_w/(\rho U)_\infty$, of 0.0, 0.01, 0.05 and 0.10 (Coupled Emission Solutions)	37
19	Nondimensional Shock Layer Velocity and Enthalpy Profiles for Coupled and Uncoupled Emission Solution with a Nondimensional Mass Injection Rate of 0.05	38
20	Comparison of Heating Rates Predicted by Three Methods for Project Fire II Trajectory	41

NOMENCLATURE

a_i	velocity profile coefficients
B	Planckian radiation intensity
c	velocity of light
$dq_r/dh\nu$	monochromatic energy flux
E	radiant emission rate
$\mathcal{E}_N$	exponential integral
f	velocity function, u/u_δ
g	enthalpy function, H/H_δ
H	total enthalpy
h	static enthalpy, also Planck constant
I_1	integral of f^2
I_2	integral of f
I_ν	local radiation intensity
k	Boltzmann constant
N_i	number density of specie i
P	static pressure
Pr	Prandtl number
$\dot{q}_c$	convective energy flux
$\dot{q}_r$	radiative energy flux
$\dot{q}_{total}$	total surface heat flux
R	radius of curvature
Re	Reynolds number, $\rho_{\delta,0} U_\infty R/\mu_{\delta,0}$
r	defined in Figure 1

T	temperature
U_∞	freestream velocity
u	velocity component parallel to body
v	velocity component normal to surface
x, y	body-oriented coordinates

Greek

α_ν	absorption coefficient
δ	shock detachment distance
$\tilde{\delta}$	transformed shock detachment distance
ϵ	difference between body and shock angle
η	Dorodnitzyn variable
θ	body angle
κ	body curvature
$\tilde{\kappa}$	$1 + \kappa y$
μ	viscosity
ν	frequency
ξ	nondimensional x-coordinate
ρ	density
$\bar{\rho}$	density ratio across shock, $\rho_\infty / \rho_{\delta,0}$
σ	effective cross section
τ_ν	optical depth at frequency ν
ϕ	shock angle
χ	$h\nu/kT$
Ω	solid angle
ω	vorticity

Subscripts

w	wall quantities
δ	quantities immediately behind the shock
∞	freestream condition
0	stagnation line

Superscript

	dimensional quantities

Section 1
INTRODUCTION

The thermal environment of a vehicle entering a planetary atmosphere at superorbital velocities is investigated for the case where convective and radiative transport mechanisms are coupled. Accurate determination of the flow field structure and the surface heat transfer are vital to the design of reliable and practical heat protection systems. The formulation presented in this report can be used for predicting coupled heat transfer distributions about an arbitrarily shaped axisymmetric blunt body entering an arbitrary planetary atmosphere at hypersonic velocities.

The regime of atmospheric flight is restricted to the laminar continuum regime and to flight conditions where thermodynamic equilibrium can be applied. The later restriction can be easily removed by adding an equation for conservation of chemical species. The basic steady Navier-Stokes equations are reduced to a form consistent with the flow around a blunted nose in a hypersonic stream by assuming that the shock layer is thin and that the viscous layer thickness and shock stand-off distance are of the same order of magnitude. The present analysis includes the effects of mass injection, radiative emission and absorption, and coupling between convection and radiation. Effects of mass injection of ablation species on the heat transfer process are not presently included.

The primary purpose of this report is to present the results of an investigation of blunt body heating for entry into earth's atmosphere and to present a full treatment of the spectral evaluation of the radiant energy transfer. The complete governing equations and solution procedures have been formulated by the authors in a previous report (Reference 1). A brief discussion of this coupled flow field analysis is presented in Section 2. The

techniques used here follow the approach Hoshizaki and co-workers (References 2 and 3) have taken in the solution of the viscous radiating blunt body problem.

The coupled shock layer solution procedure presented in Reference 1 has been programmed for a digital computer (Reference 4) utilizing the thermodynamic and transport properties of air as computed by Hansen (Reference 5). The methods used to evaluate the spectral absorption coefficients are given in Section 3. Numerical solutions were obtained for a variety of flight conditions and Section 4 presents a discussion of these results.

Section 2
COUPLED FLOW FIELD ANALYSIS

2.1 GOVERNING EQUATIONS

The purpose of this analysis is to obtain a direct solution to the viscous blunt-body problem for the case where convective and radiative transport mechanisms are coupled. The equations used to describe the coupled flow field are a coupled set obtained from the total conservation equations for a multi-component continuum gas (References 6 and 7). The following basic assumptions are made in order to obtain a system of parabolic partial differential equations correct to the order of the density ratio across the shock.

- the shock layer is assumed to be thin, $\delta'/R' << 1$
- the thickness of the viscous layer, and the shock detachment distance are taken to be of the same order of magnitude
- terms which are of $O(\bar{\rho}^2)$ and higher have been consistently neglected

The equations used in this analysis are thus valid for a thin shock layer which is completely viscous and in thermodynamic equilibrium.

The body oriented coordinate system used in writing the coupled flow field equations is shown in Figure 1. The complete system of governing differential equations correct to $O(\bar{\rho})$ can be written as follows

X-Momentum

$$\frac{r'}{r'_w}\rho'\tilde{\kappa}'\left[u'\frac{\partial u'}{\partial x'} + \tilde{\kappa}'v'\frac{\partial u'}{\partial y'} + \kappa' u' v'\right] \tag{1}$$

$$= -\frac{\partial P'}{\partial x'} + \frac{\partial}{\partial y'}\left[\frac{r'}{r'_w}\tilde{\kappa}'^2\mu'\frac{\partial u'}{\partial y'} - \kappa'\mu' u'\right]$$

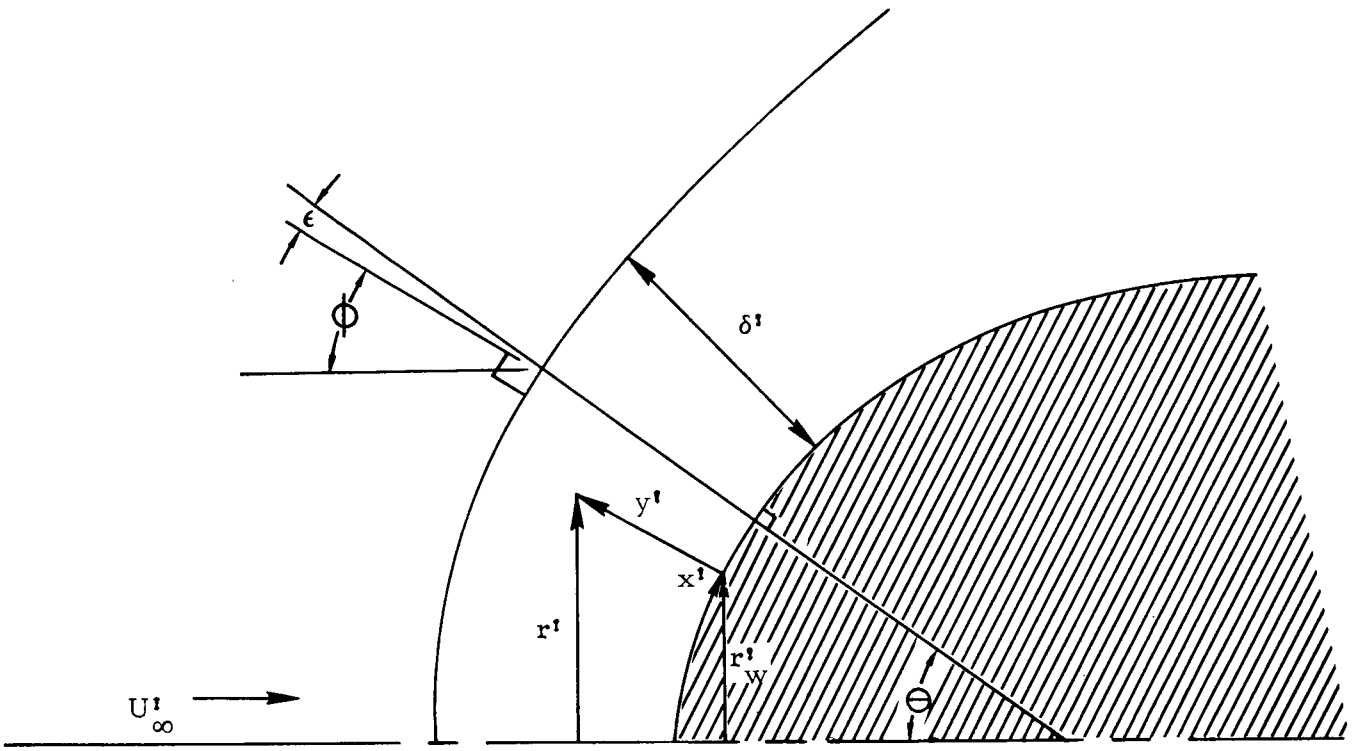

Figure 1 – Body-Oriented Coordinate System

Y-Momentum

$$\frac{r'}{r'_w}\rho'\left[u'\frac{\partial v'}{\partial x'}+v'\frac{\partial v'}{\partial y'}-\frac{\kappa'}{\tilde{\kappa}'}u'^2\right]=-\frac{\partial P'}{\partial y'} \tag{2}$$

Continuity

$$\frac{\partial}{\partial x'}(r'\rho'u')+\frac{\partial}{\partial y'}(\tilde{\kappa}'r'\rho'v')=0 \tag{3}$$

Energy

$$\frac{r'}{r'_w}\rho'\left[u'\frac{\partial H'}{\partial x'}+\tilde{\kappa}'v'\frac{\partial H'}{\partial y'}\right]-\frac{\partial}{\partial y'}\left[\tilde{\kappa}'\frac{r'}{r'_w}\frac{\mu'}{Pr}\frac{\partial h'}{\partial y'}\right]$$

$$=\frac{\partial}{\partial y'}\left[\left(\frac{r'}{r'_w}+2\kappa'y'\right)\frac{\mu'}{\kappa'}u'\frac{\partial u'}{\partial y'}\right]-\frac{\partial}{\partial y'}\left[\kappa'\mu'u'^2\right]-\tilde{\kappa}'\frac{r'}{r'_w}E' \tag{4}$$

The radiative term E' that appears in the energy equation, Equation (4), represents the volumetric rate of emission or absorption of energy by the shock layer gas due to radiation. Two assumptions are made in this analysis in order to evaluate this radiation transport term in a practical manner.

- the shock layer geometry is approximated by a semi-infinite plane slab
- the shock layer is assumed to be locally one-dimensional in that radiation transport influence is allowed in only one direction.

It has been shown previously (Reference 8) that this one-dimensional plane slab model can be used to obtain quantitatively valid results. The radiation flux divergence can be written

$$-E' = \int_0^\infty \alpha_\nu \left[\int_\Omega I_\nu \, d\Omega - 4\pi B_\nu \right] d\nu \tag{5}$$

where α_ν is the spectral absorption coefficient, I_ν is the local intensity, B_ν is the Planckian radiation intensity and Ω is a surface solid angle.

A detailed mathematical analysis of Equation (5) is presented in Reference 1 where the following expression for the radiative flux divergence is derived.

$$-E' = \int_0^\infty 2\pi \alpha_\nu \left[\int_0^{\tau_\nu} B_\nu \, \mathcal{E}_1 (\tau_\nu - \hat{\tau}_\nu) \, d\hat{\tau}_\nu + \int_{\tau_\nu}^{\tau_{\nu,s}} B_\nu \, \mathcal{E}_1 (\hat{\tau}_\nu - \tau_\nu) \, d\hat{\tau}_\nu - 2 B_\nu \right] d\nu \tag{6}$$

In equation (6), τ_ν is the optical depth at frequency ν given by

$$\tau_\nu = \int_0^{y'} \alpha_\nu \, dy' \tag{7}$$

B_ν is Planckian intensity which can be written

$$B_\nu = \frac{2 h \nu^3}{c^2} \left[\frac{1}{\exp(h\nu/kT) - 1} \right] \tag{8}$$

and $\mathcal{E}_1$ is the exponential integral.

The system of equations, Equations 1-8, defines the radiation-coupled flow field used in this analysis of blunt body heating. The following subsection presents a brief discussion of the method used to solve this system.

2.2 METHOD OF SOLUTION

The equations used in this analysis are solved numerically, using a combination of integral methods and successive approximation techniques. Solutions to the momentum equation will be obtained in a numerical manner using an integral technique much like the Karman-Pohlhausen method for boundary layer analysis. The energy equation is solved by a successive approximations technique, utilizing finite-difference methods for approximation of streamwise derivatives.

The momentum equation is first integrated across the shock layer to obtain an integro-differential equation in one independent variable. The shock layer gas velocity profile is then assumed to be representable by polynomials with sufficient boundary conditions being specified to uniquely define this polynomial. This type of method has been used by Maslen and Moeckel (Reference 9) and by Hoshizaki and Wilson (Reference 3) and this analysis closely follows their work.

The energy equation is solved by a finite-difference, successive approximations technique. Equation (4) is manipulated into a form suitable for a numerical iteration procedure which is started by an initial guess for the shock layer enthalpy profile. This estimated profile is then used in determining the thermodynamic, transport and radiative properties of the gas mixture. Solutions to the energy equation can then be obtained, compared to the initial guess, and iterated until satisfactory convergence is obtained.

The conservation equations as stated in Equations (1) through (4) are in the body oriented (x, y) coordinate system (Figure 1). They will actually be solved in a dimensionless (ξ, η) coordinate system, where

$$\xi = \frac{x'}{R'}, \qquad \eta = \frac{1}{\tilde{\delta}'} \int_0^{y'} \frac{r'}{r'_w} \rho' \, dy' \tag{9}$$

In this analysis all variables are non-dimensionalized according to the scheme presented in Reference 1. The dimensionless transformed equations have the following form.

Momentum Integro-Differential Equation

$$u_\delta \frac{dI_1}{d\xi} + \left[2 \frac{du_\delta}{d\xi} + \tilde{\kappa}_\delta \frac{u_\delta}{r_w} \frac{dr_w}{d\xi} \right] I_1 = \frac{r_\delta}{r_w} \rho_\delta u_\delta \frac{d\delta}{d\xi}$$

$$+ \tilde{\delta}^2 u_\delta \frac{d\kappa}{d\xi} \int_0^1 f^2 \left[\int_0^\eta \frac{d\bar{\eta}}{\rho} \right] d\eta - \tilde{\kappa}_\delta \left(\frac{r_\delta}{r_w} \right) \rho_\delta v_\delta - \delta \bar{\rho} \frac{1}{u_\delta} \left(\frac{\partial P}{\partial \xi} \right)_\delta \tag{10}$$

$$+ \frac{1}{\tilde{\delta} Re} \left[\tilde{\kappa}_\delta (\rho \mu)_\delta \left(\frac{r_\delta}{r_w} \right)^2 \left(\frac{\partial f}{\partial \eta} \right)_{\eta=1} - \tilde{\delta} \kappa \mu_\delta - (\rho \mu)_w \left(\frac{\partial f}{\partial \eta} \right)_{\eta=0} \right]$$

Transformed Energy Equation

$$\frac{\partial}{\partial \eta} \left[\frac{\rho \mu}{Pr} \left(\frac{r}{r_w} \right)^2 \tilde{\kappa} \frac{\partial g}{\partial \eta} \right] + \tilde{\delta} Re \left[u_\delta \frac{\partial I_2}{\partial \xi} + \left(\frac{du_\delta}{d\xi} + \frac{u_\delta}{r_w} \frac{dr_w}{d\xi} \right) I_2 - \bar{\rho} (\rho v)_w \right] \frac{\partial g}{\partial \eta} =$$

$$Re \, \tilde{\delta}^2 u_\delta f \frac{\partial g}{\partial \xi} + \frac{\partial}{\partial \eta} \left[(\rho \mu) \tilde{\kappa} \left(\frac{r}{r_w} \right)^2 \left(\frac{1}{Pr} - 1 \right) \frac{U'^2_\infty}{H'_\delta} u_\delta^2 f \frac{\partial f}{\partial \eta} \right] \tag{11}$$

$$+ \frac{U'^2_\infty}{H'_\delta} u_\delta^2 \tilde{\delta} \kappa \frac{\partial}{\partial \eta} (\mu f^2) + \tilde{\kappa} \tilde{\delta}^2 Re \, \bar{\rho} \left(\frac{\rho'_\delta}{\rho'} \right) \frac{U'^2_\infty}{H'_\delta} E \, .$$

In order to approximate the velocity profile by a fifth-order polynomial

$$\frac{u}{u_\delta} = f(\xi, \eta) = \sum_{i=0}^{5} a_i(\xi)\, \eta^i \tag{12}$$

the following boundary conditions are chosen:

- $u = 0$ at $y = 0$
- $u = u_\delta$ at $y = \delta$
- $\frac{\partial^2 u}{\partial y^2} = 0$ at $y = \delta$
- Momentum equation evaluated at body surface
- Total mass balance
- $\omega = \omega_\delta$ at $y = \delta$

The shock boundary conditions are the Rankine-Hugoniot relations which can be written

$$\begin{aligned} v_\delta &= \sin\phi \sin\epsilon - \bar{\rho} \cos\phi \cos\epsilon \\ u_\delta &= \sin\phi \cos\epsilon + \bar{\rho} \cos\phi \sin\epsilon \\ P_\delta &= (1 - \bar{\rho}) \cos^2\phi \end{aligned} \tag{14}$$

The two boundary conditions necessary to solve the energy equation are

$$g(0) = g_w ,$$

$$g(1) = 1 .$$

The objective of this study is to obtain coupled heating rate distributions about a blunt body in a hypersonic flow field. The following expressions are used in the (ξ, η) coordinate system to yield these surface heating rates.

Convective:

$$q'_c = - \left(\frac{\rho\mu}{Pr}\right)_w \frac{\rho'_\infty U'^3_\infty}{2\tilde{\delta}\, Re\, \bar{\rho}} \left(\frac{\partial g}{\partial \eta}\right)_w \cdot$$

Radiative: (15)

$$q'_r = - \int_0^\infty \int_0^{\tau_{\nu,\delta}} \frac{4\pi\, h\nu^3}{c^2 \left[\exp(h\nu/kT) - 1\right]} \mathcal{E}_2(t)\, dt\, d\nu \,.$$

Details of the numerical solution procedure will not be presented in this report, and the interested reader is referred to Reference 1 for more information on the techniques.

Section 3
GAS PROPERTIES

3.1. THERMODYNAMIC AND TRANSPORT PROPERTIES

The formulated method outlined in the previous section is applicable to arbitrary gases; however, for this analysis only the species of air are considered. Equilibrium thermodynamic and transport properties of air were obtained from a closed form set of approximate partition functions for the major components of air (Reference 5). The partition functions were programmed (Reference 10) such that the total number densities, enthalpy, viscosity, Prandtl number and specie concentrations could be found for a given temperature and pressure. Since the independent variables of this analysis are enthalpy and pressure rather than temperature and pressure, an iteration scheme (Reference 4) was used to obtain equilibrium properties as a function of enthalpy and pressure.

The equilibrium species number densities are important values used in the radiation calculation. For this reason, number densities from the approximate partition functions were compared (Figure 2) with number densities from the FEMP computer program. The FEMP program (Reference 11) is a free energy minimization computer program which calculates the equilibrium thermodynamic properties of gases. The number densities which were calculated using the two methods for a pressure of .68 atm and a temperature range of 2000 to 14000°K agree very well. This agreement is typical and lends validity to the use of the species number densities as well as the overall thermodynamic properties obtained from the approximate partition functions of Reference 5.

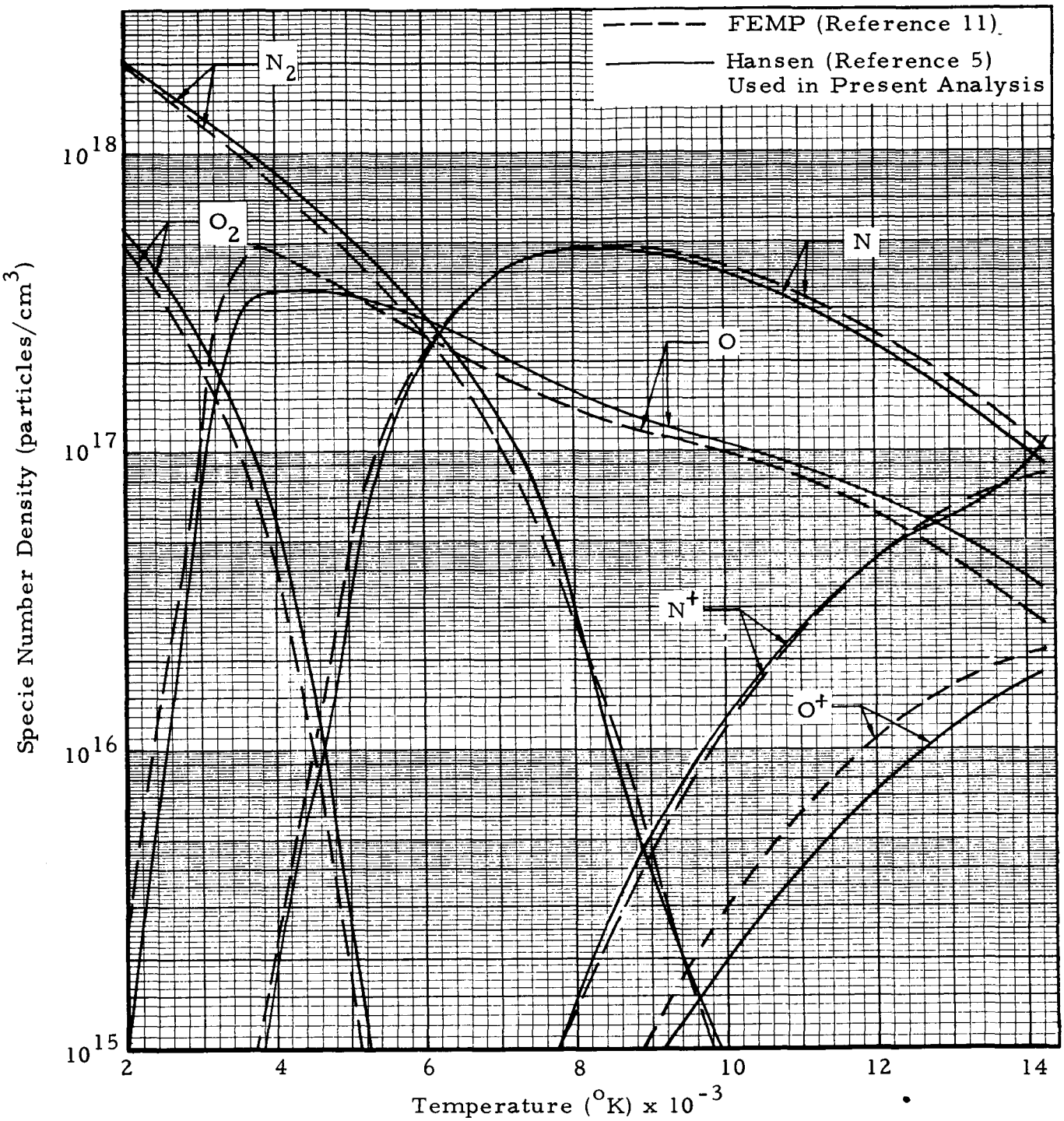

Figure 2 - Comparison of Specie Number Density Versus Temperature Calculated Using Two Methods for a Pressure of .68 atm

3.2 RADIATIVE PROPERTIES

Two methods were used to evaluate the radiative properties of air. These properties determine the radiative heat transfer within a shock layer. The amount of heat transfer by radiation is dependent on the radiative flux divergence, E', at each point in the shock layer. The radiative flux divergence is a direct integral function of the absorption coefficient of the gas species. Further, the absorption coefficient is a complex function of the temperature, radiation frequency, types of species present and specie number density. Because of the overall complexity of evaluating radiative properties, both a simple and a detailed method were used. One method involves using curve fits of radiative emission in air, and the other method involves detailed evaluation of spectral absorption coefficients.

A simple model for the continuum radiation flux divergence in air, based on the work of Yos (Reference 12), was used to obtain coupled radiative and convective heating solutions. Yos presents a family of curves for the continuum radiative flux divergence as a function of temperature and pressure. This family of curves is adequately represented by the curve fit equations listed below.

$$T_t = 1100 \log_{10} P + 13800$$

If $T < T_t$, then

$$\log_{10} E' = 0.0005T + 1.15 \log_{10} P - 3.15 \qquad (16)$$

or, if $T \geq T_t$, then

$$\log_{10} E' = 1.875 \log_{10} P + 3.903$$

where T is the temperature in ^{o}K, P is the pressure in atmospheres, and E' is the continuum radiative flux divergence in watts/cm^3. This model overestimates the radiative flux because only emission (i.e., no self-absorption) is considered. The principal advantage of using this model is that it permits coupled solutions to be obtained rapidly.

Detailed calculations of the radiative flux divergent term must be carried out in most flight regimes and where significant amounts of ablation products are introduced into the shock layer. The flux divergent term, Equation (6), was evaluated using spectral absorption coefficients, α_ν, from References 3 and 8. The spectral absorption coefficients of individual species are defined in terms of radiation cross section, σ_ν, by the equation

$$(\alpha_\nu)_i = N_i (\sigma_\nu)_i \tag{17}$$

where N is the specie number density in particles/cm^3. The total absorption cross section for air at a particular frequency can be written

$$\alpha_\nu = (1 - e^{-X}) \sum_{i=1}^{n} (\alpha\nu)_i \tag{18}$$

where the term in front of the summation accounts for induced emission, $X = h\nu/kT$, and n is the number of species. Thus, in order to determine the spectral absorption coefficient, the radiation cross section of each specie must be found.

The method of determining radiative cross sections of major contributing species follows the work of Hoshizaki and co-workers (References 3 and 8). The reader is referred to these references for specific details of models used to determine these cross sections. Typical cross-section curves for the six contributing species in air are shown in Figures 3 through 6. Figures 3 and 4 present continuum cross section variations with frequency due to bound-free and

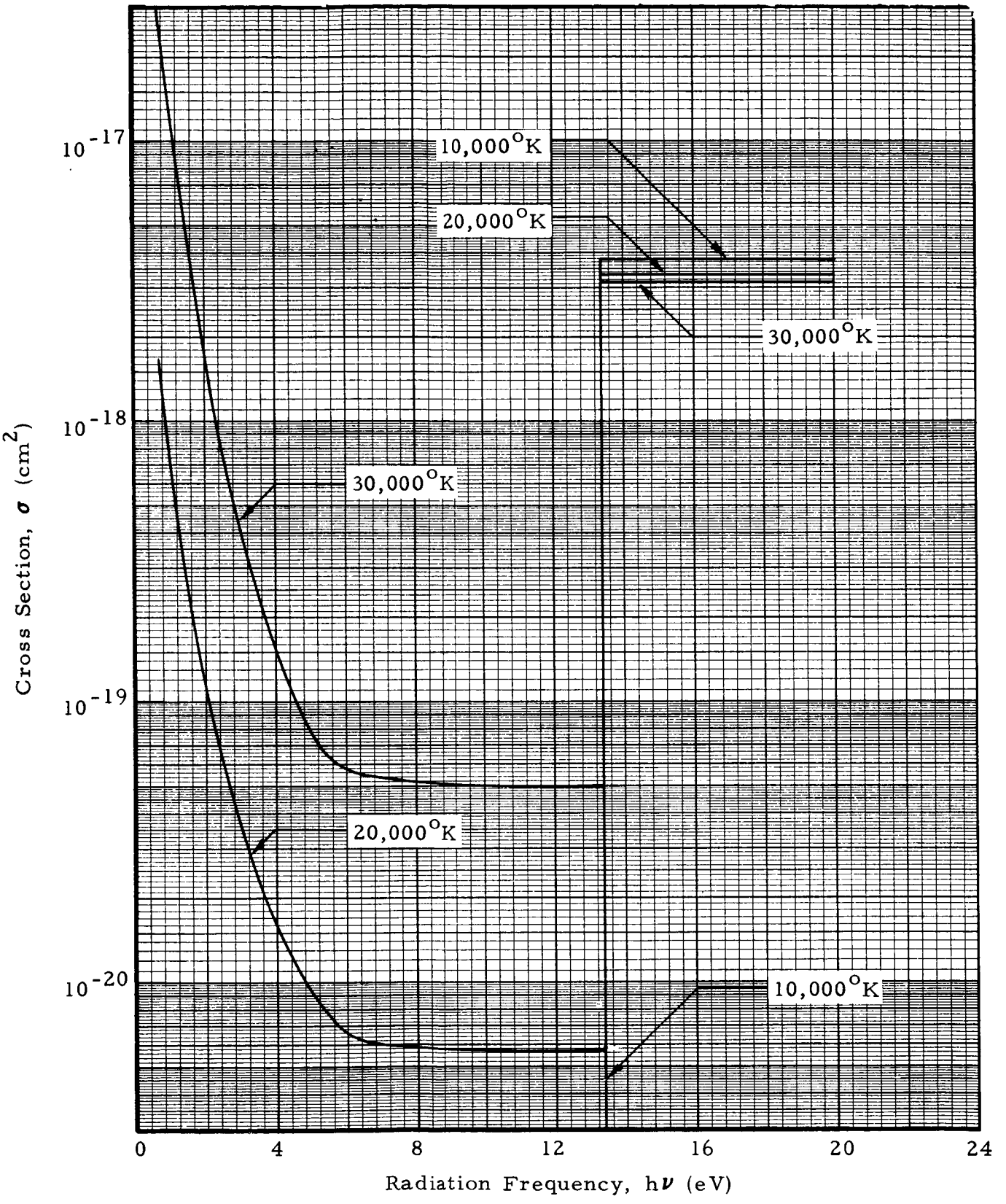

Figure 3 - Radiative Cross Section of O Atoms as a Function of Frequency for Three Temperatures

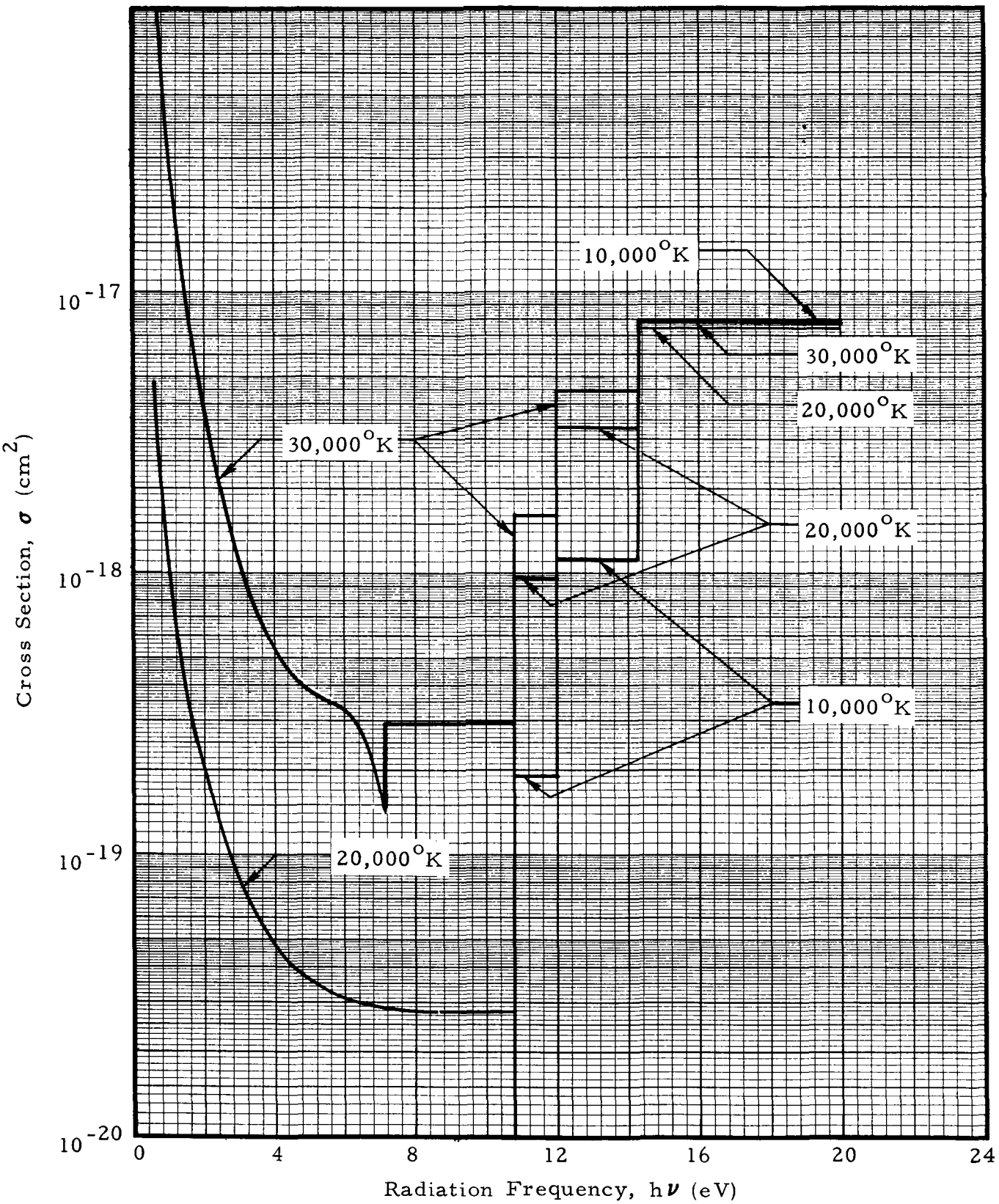

Figure 4 - Radiative Cross Section of N Atoms as a Function of Frequency for Three Temperatures

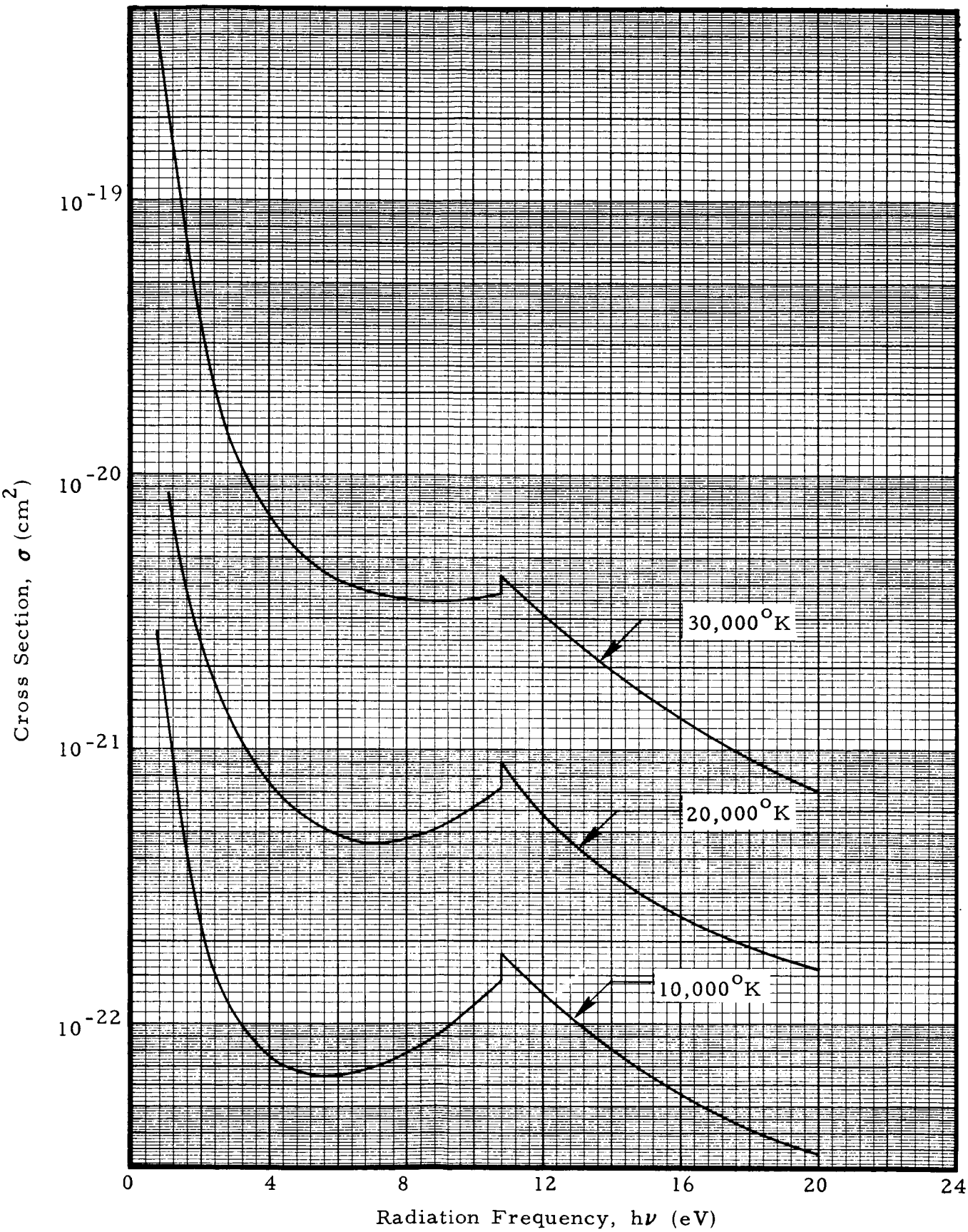

Figure 5 - Radiative Cross Section of N^+ and O^+ as a Function of Frequency for Three Temperatures

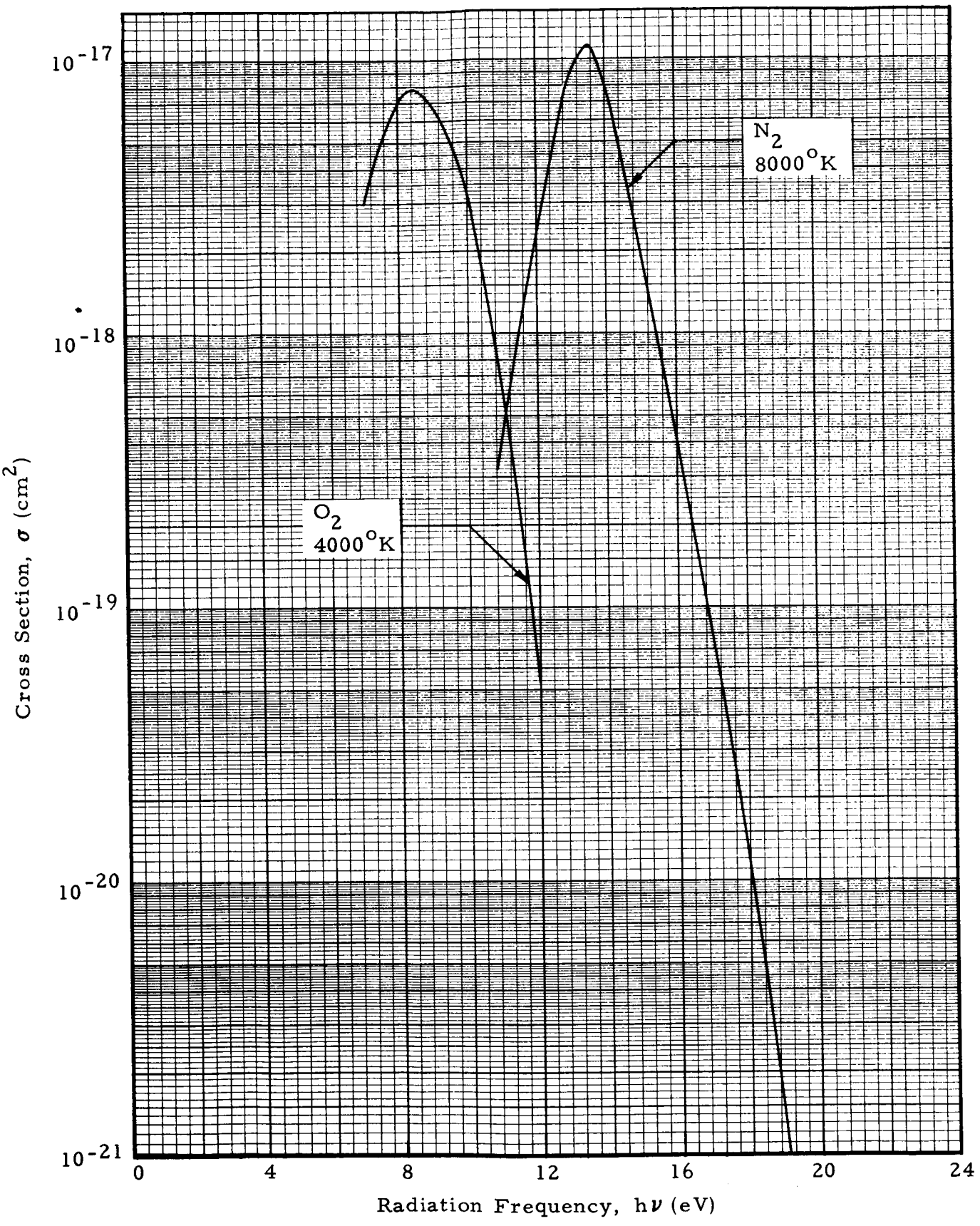

Figure 6 - Radiative Cross Section of N_2 and O_2 Molecules as a Function of Frequency

free-free transitions for O atoms and N atoms, respectively. Figure 5 presents typical continuum cross sections for N^+ and O^+, where the cross section of O^+ is assumed equal to that of N^+. This is an acceptable approximation because the ions contribute little to the total absorption coefficient except at high frequencies where the radiation from the shock layer is near that of a black body (Reference 3). The only significant molecular absorption coefficients of air are the O_2 Schumann-Runge continuum and the N_2 Birge-Hopfield band (Reference 3). Typical cross sections for the two molecules are shown in Figure 6. Upon obtaining the significant radiative cross sections of air, the total absorption coefficient and thus the radiative flux emission term can be evaluated.

Section 4
RESULTS AND DISCUSSION

4.1 EMISSION AND SPECTRAL ABSORPTION MODEL RESULTS

Solutions of the shock layer equations using the techniques described in the previous sections provide insight into the coupled radiative and convective heat transfer mechanisms through real gases. The radiative emission and the spectral absorption models presented in this analysis yield different results whether coupled or uncoupled to the convective heat transfer mechanism.

Results obtained by using the spectral model, which is based on realistic absorption coefficients, and the emission model are shown in Figures 7 and 8 for the same flight conditions. Figure 7 presents two sets of curves — one for shock layer pressure profiles and one for temperature profiles. The shock layer pressure profile is seen to be a monotonic increasing function for both a coupled and an uncoupled solution. The emission model and the spectral absorption model yield the same pressure profile, to four significant figures, in a radiative coupled solution. Radiative coupling produces a larger change in the shock layer temperature profile than in the pressure profile. Coupling increases the thermal thickness and decreases the shock layer thickness (Figure 7). The inflection point in the temperature profile near $\eta = 0.1$ is due to the dissociation of N_2. Further, the coupled solutions for both radiation models yield about the same shock layer temperature profile.

Figure 8 presents radiative emission profiles for both coupled and uncoupled solutions using the two radiation models. Radiation coupling produces a very significant change in emission profiles for both models. Further, both radiation models produce distinctively different shock layer emission profiles whether they are uncoupled or coupled solutions. The main distinction is that the detailed spectral model includes the effects of

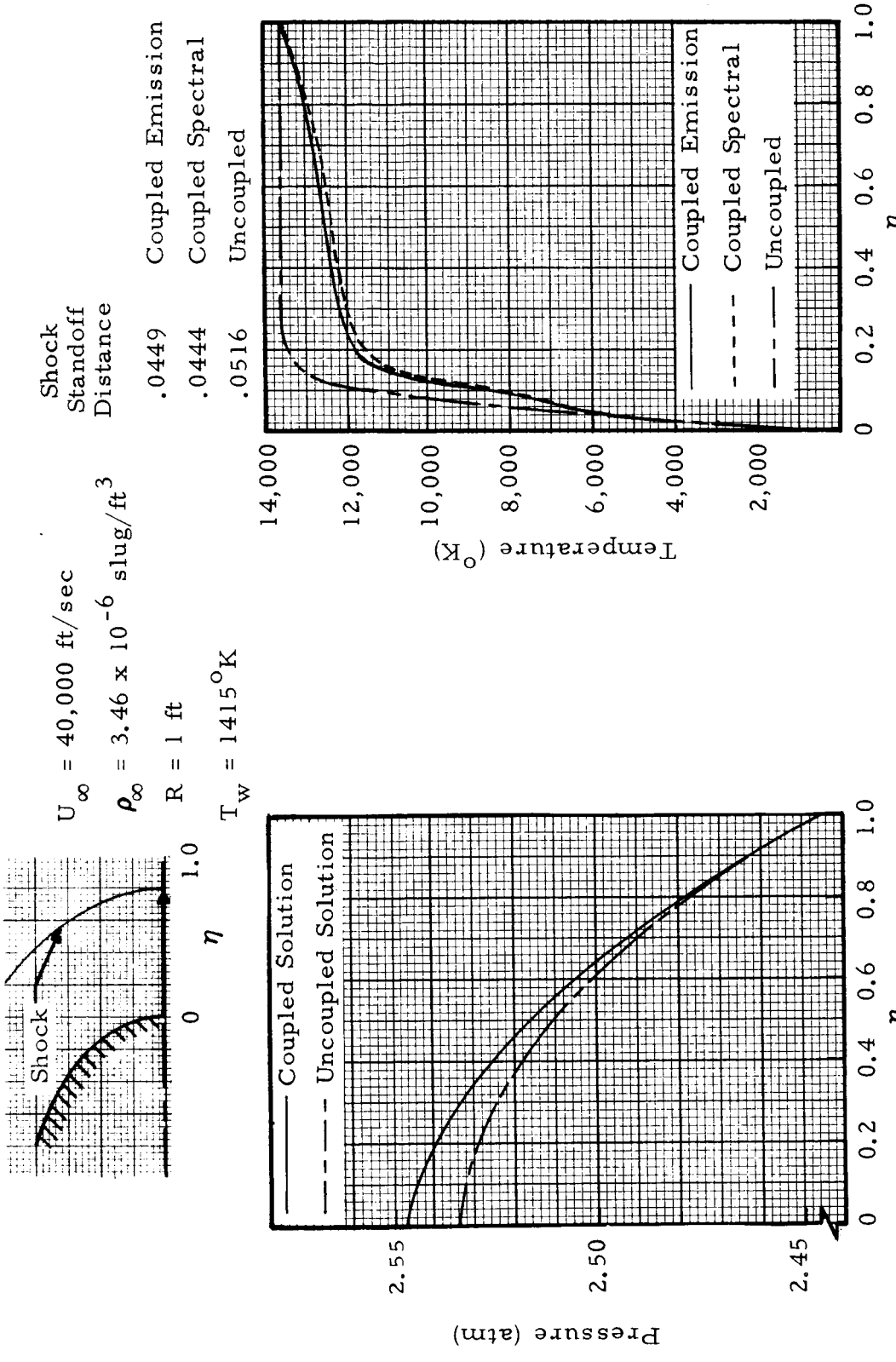

Figure 7 - Shock Layer Pressure and Temperature Profiles

U_∞ = 40,000 ft/sec

ρ_∞ = 3.46 x 10^{-6} slug/ft^3

R = 1 ft

T_w = 1415°K

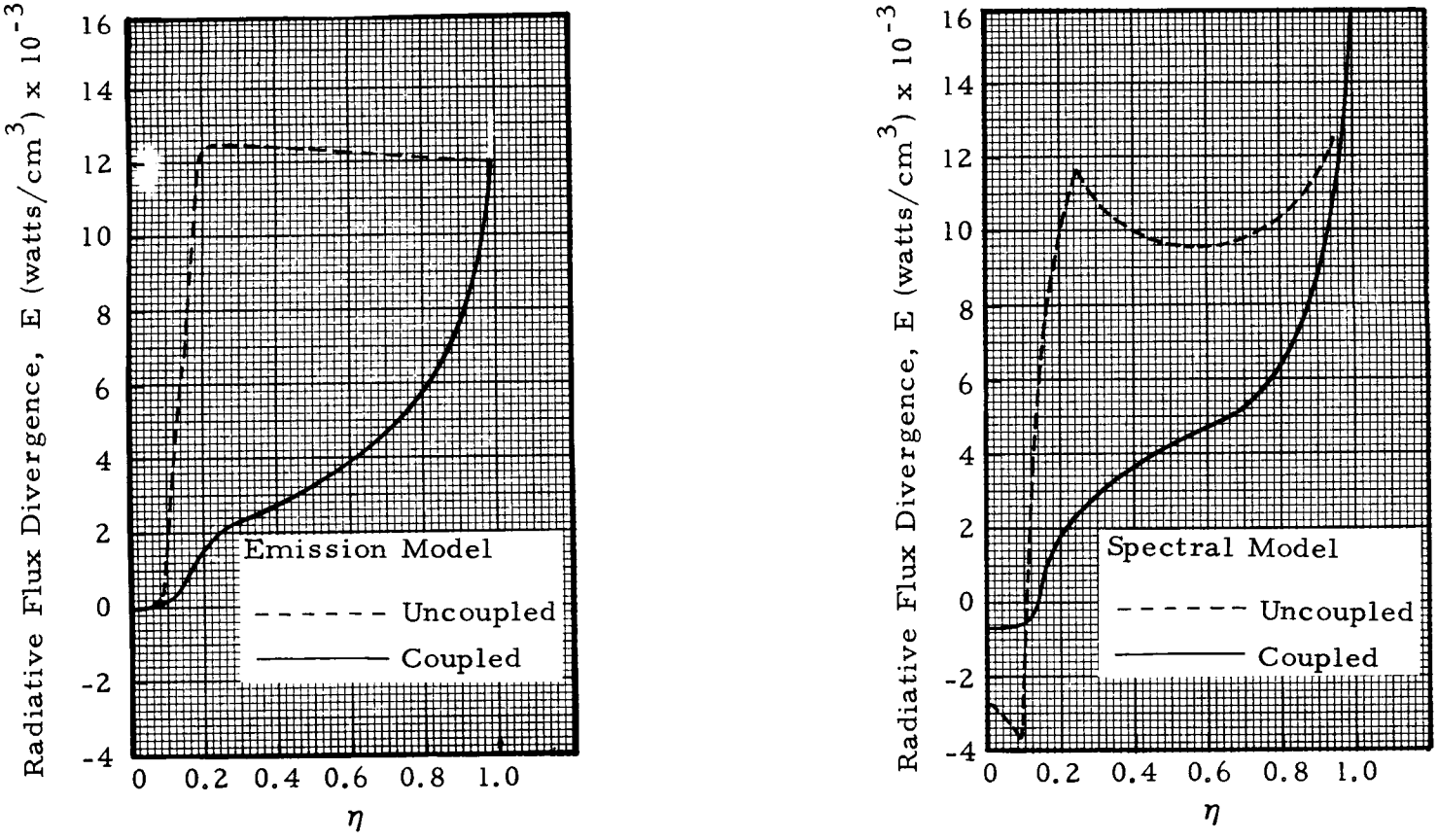

Figure 8 - Radiative Flux Divergence, E, Profiles Obtained from the Spectral and Emission Models

absorption and this yields negative emission values near the wall. Both radiation models yield emission profiles which are very sensitive to temperature and to a lesser extent to pressure. Thus, to obtain realistic radiative emission, an accurate temperature distribution must be obtained and it, of course, is a function of the radiative emission such that the problem is coupled.

The detailed spectral radiation model provides more insight than the emission model into the mechanisms of coupled radiative and convective heat transfer. The detailed spectral radiation model is based on obtaining realistic absorption cross sections, as described in Section 3.2, and thus is based on computing realistic absorption coefficients from Equation (18). Absorption coefficients as a function of frequency for typical wall and shock conditions are presented in Figures 9 and 10, respectively.

The monochromatic optical depth, which is based on the absorption coefficients [Equation (7)], for several frequencies is shown in Figure 11. These results show that the shock layer gas is highly absorbing in the vacuum ultraviolet ($h\nu \geq 13$) and nearly transparent in the visible ($h\nu \cong 10$) and infrared ($h\nu \cong 1.0$) part of the spectrum as indicated by References 3 and 8. The monochromatic energy flux, $\partial \dot{q}_r / \partial h\nu$, at the wall corresponding to the optical depths shown in Figure 11, is presented in Figure 12. It is interesting to note that radiative coupling changes the character of the profile, as well as decreases the magnitude of the monochromatic energy flux.

To determine the usefulness of the radiative models, the range of applicability, and for comparison with existing correlation equations, Figure 13 was prepared. This figure presents the total heating rate as a function of freestream velocity for three freestream densities which are of different orders of magnitude. Three methods were used to calculate heating rates for comparison. The three methods were (1) a coupled solution using the emission model, (2) a coupled solution using the detailed spectral model,

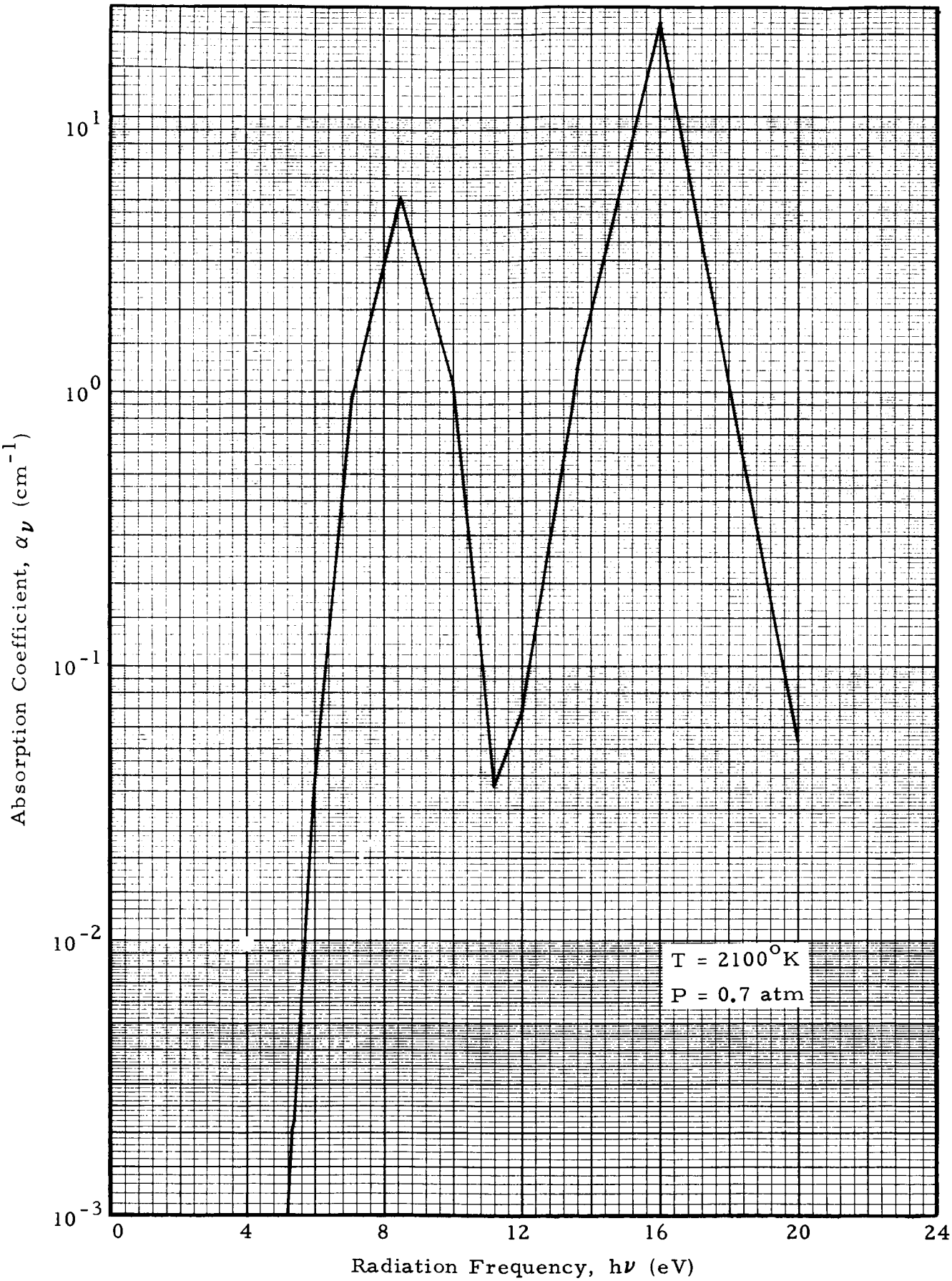

Figure 9 - Absorption Coefficient Versus Frequency for a Typical Wall Condition

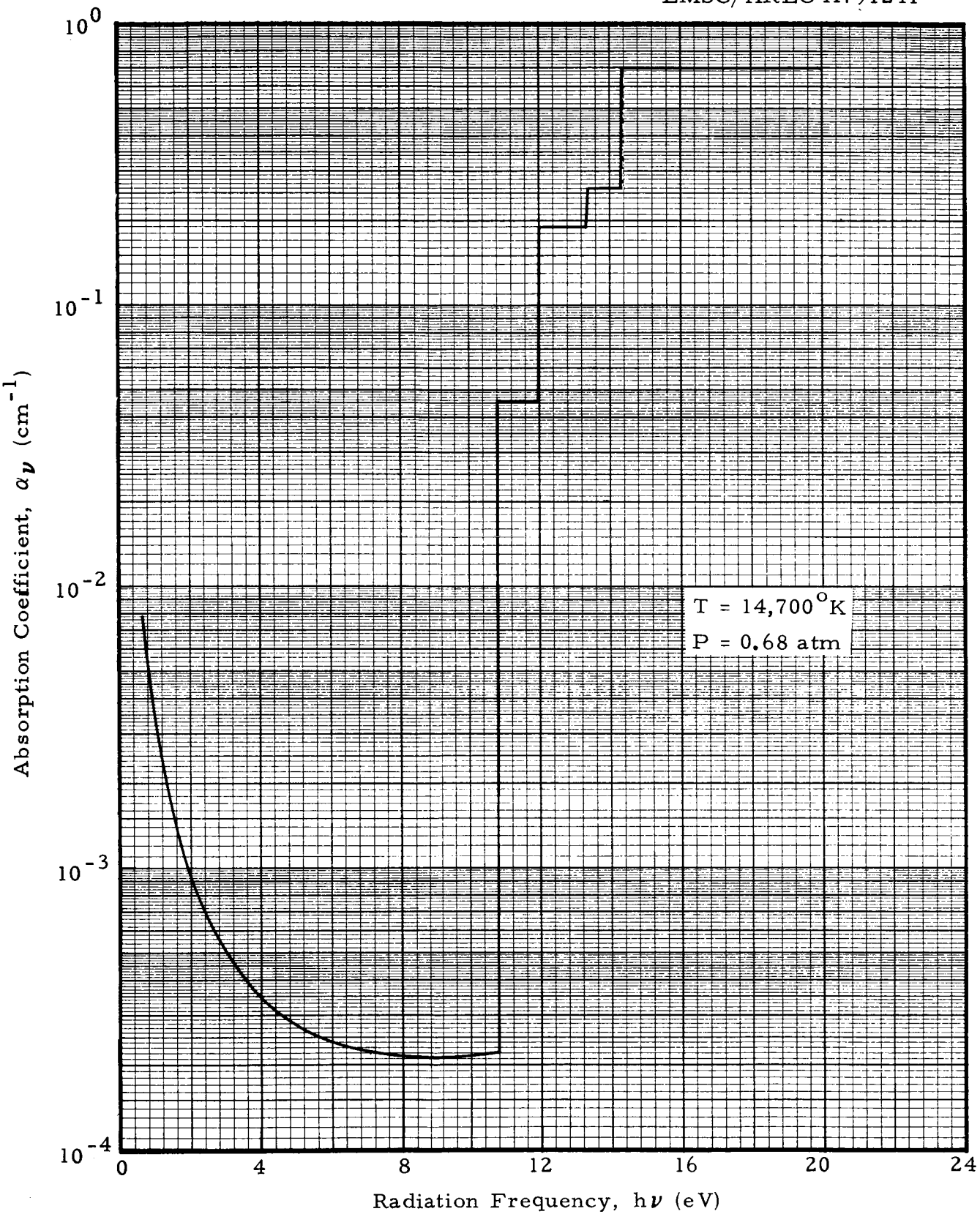

Figure 10 - Absorption Coefficient Versus Frequency for Typical Conditions Behind a Shock

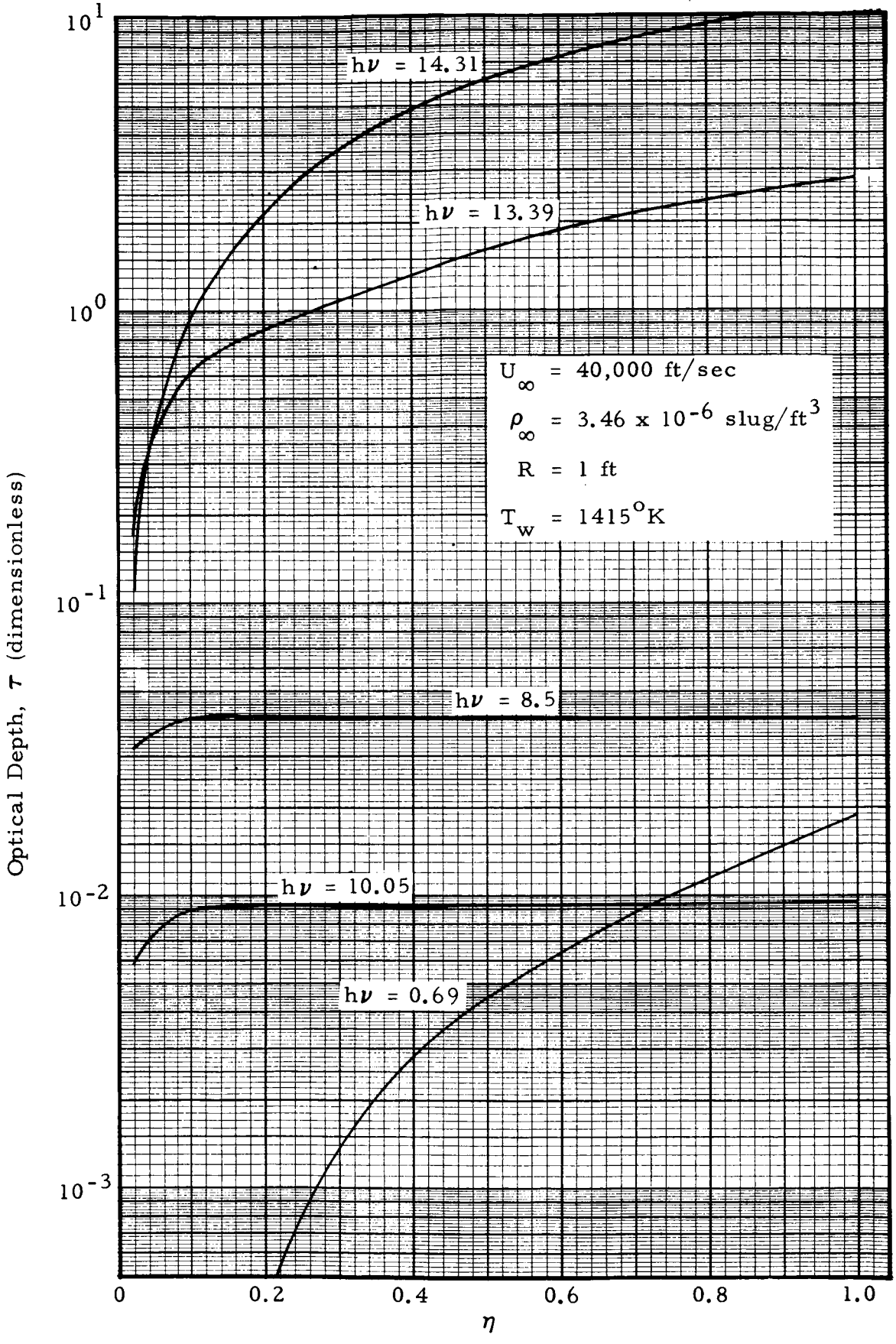

Figure 11 - Optical Depth Versus Nondimensional Shock Layer Coordinate for Five Typical Frequencies

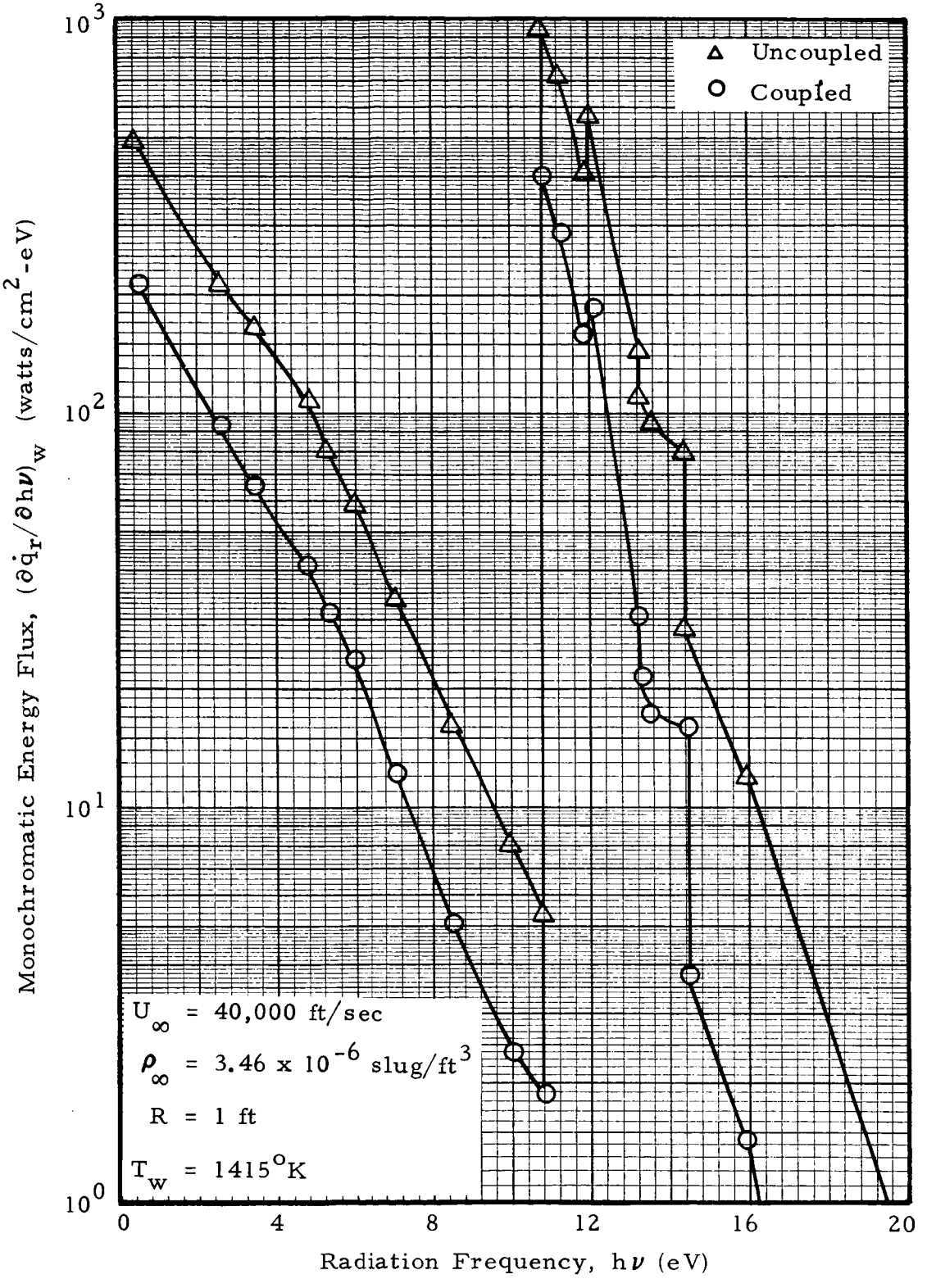

Figure 12 - Monochromatic Energy Flux at the Wall Versus Frequency for a Coupled and Uncoupled Solution

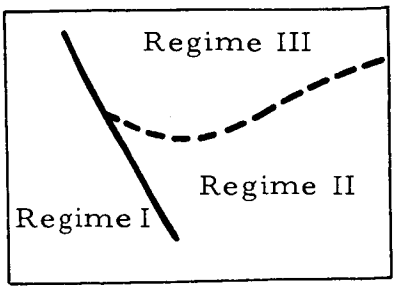

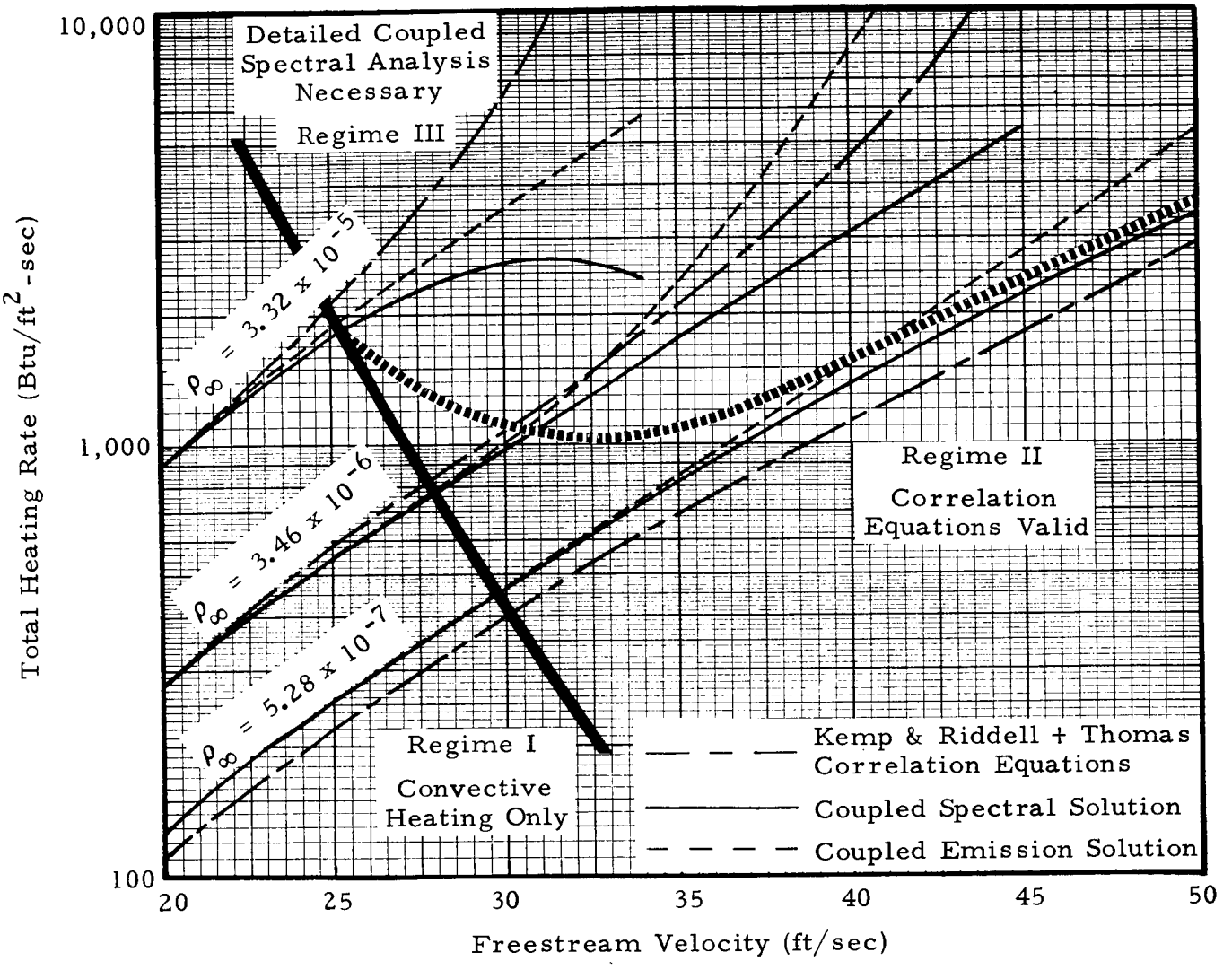

Figure 13 - A Comparison of Total Heating Rates Versus Freestream Velocity for Three Freestream Densities (R = 1 ft)

and (3) an uncoupled solution obtained by simply adding the convective heating rate predicted by the correlation equation of Kemp and Riddell (Reference 13) and the radiative heating rate predicted by the correlation equation of Thomas (Reference 13). The results presented in Figure 13 indicate there are three density-velocity regimes in which heating rates should be calculated by different methods. The first regime consists of the lower velocities. Detailed calculations of the present study and the correlation equation of Kemp and Riddell are in good agreement — note there is no radiation contribution. Obviously, for the sake of simplicity, the correlation equation should be used in this regime. The second regime includes higher velocities but is limited to lower freestream densities. In this regime, detailed calculations of this study using both radiation models agree with results obtained by adding heating rates from the correlation equation of Kemp and Riddell and the correlation equation of Thomas. Again, the correlation equations should be used in this regime where little radiative coupling occurs. In the third regime, the radiative and convective heat transfer mechanisms are strongly coupled. A detailed calculation of heating rates based on a realistic radiation model is essential to obtain valid heating rates. Figure 13 shows that both the correlation equations and the calculations based on the emission model yield heating rates much higher than those predicted by the detailed flowfield solution, including realistic effects of self absorption.

An additional interesting feature is shown in Figure 13. The heating rate curve for the coupled spectral analysis at a freestream density of $\rho_\infty = 3.32 \times 10^{-5}$ slug/ft^3 shows a maximum. This unusual behavior can be explained by first observing the shock layer temperature distribution (Figure 14) for $U_\infty = 34{,}000$ ft/sec. The energy in the shock layer is distributed due to radiative and convective coupling, such that approximately 80% of the shock layer is near the ionization temperature of nitrogen. This is shown by the specie concentration profiles presented in Figure 14. Further, the contribution of N atoms to the absorption cross section is significantly greater than N^+ ions. (See Figures 4 and 5.) Also, the shock layer pressure is approximately 17 atmospheres. This combination significantly increases the absorption coefficient such that the optical depths

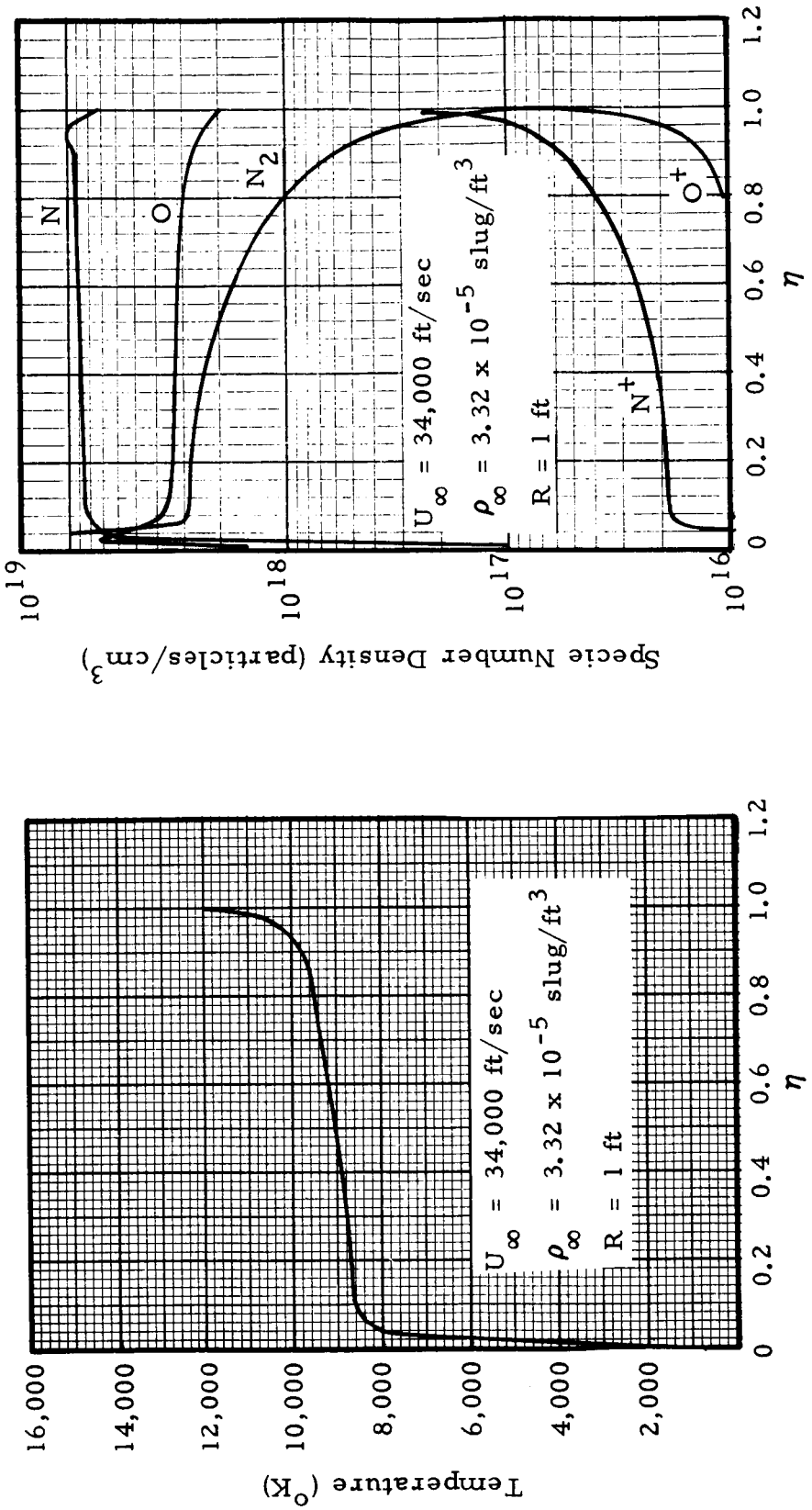

Figure 14 - Shock Layer Temperature and Specie Number Density Profiles for a Flight Condition Producing Strong Radiation Coupling

are increased by an order of magnitude over those, for example, shown in Figure 11. The net result is that the shock layer gas radiates like a black body at a temperature of approximately 8800°K and thus decreases the radiative heating flux to the surface very significantly. Thus, one arrives at the paradoxical conclusion that an increase in velocity at a constant altitude reduces the stagnation point heating rate in certain flight regimes. However, before making any such sweeping conclusions, it must be recognized that this flight condition (34,000 ft/sec at an altitude of approximately 100,000 ft) is unrealistic and hence the present method perhaps neglects certain effects which play a dominant role for this unusual flight condition. One such effect is percursor radiation, a field in which only a small amount of detailed work has been done.

In reference to the usefulness and applicability of the spectral and emission models, two additional points should be made. First, as the body radius of a vehicle increases beyond one foot, the velocity-density regime in which correlation equations can be used is significantly reduced. This is shown in Figure 15 and will be further demonstrated in Section 4.2. As a result, a coupled solution using a detailed spectral model is needed over a larger velocity-density regime for large body radii than for small body radii. Secondly, the emission model appears to be useful only in determining trends and not for quantitative work. The emission model can be of practical value, because it permits coupled solutions to be obtained rapidly. A coupled solution using the emission model required approximately eight seconds execution time on a Univac 1108, whereas a coupled solution using the spectral model requires approximately 50 seconds. In some flight regimes the initial guess for the enthalpy is rather critical when using the spectral model. To obtain a good guess for a coupled solution using the spectral model, a coupled solution using the emission model for a similar problem can be used. This is accomplished by stacking the problems back to back for input into the computer program (Reference 4) developed using the present analysis. This technique eliminates many initial guessing problems and reduces the execution time by approximately 18 seconds for solutions using the spectral model.

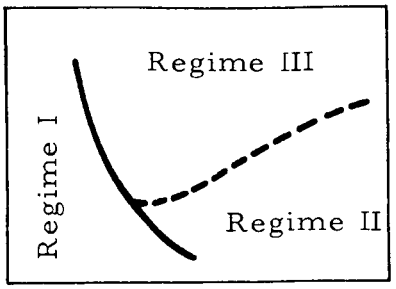

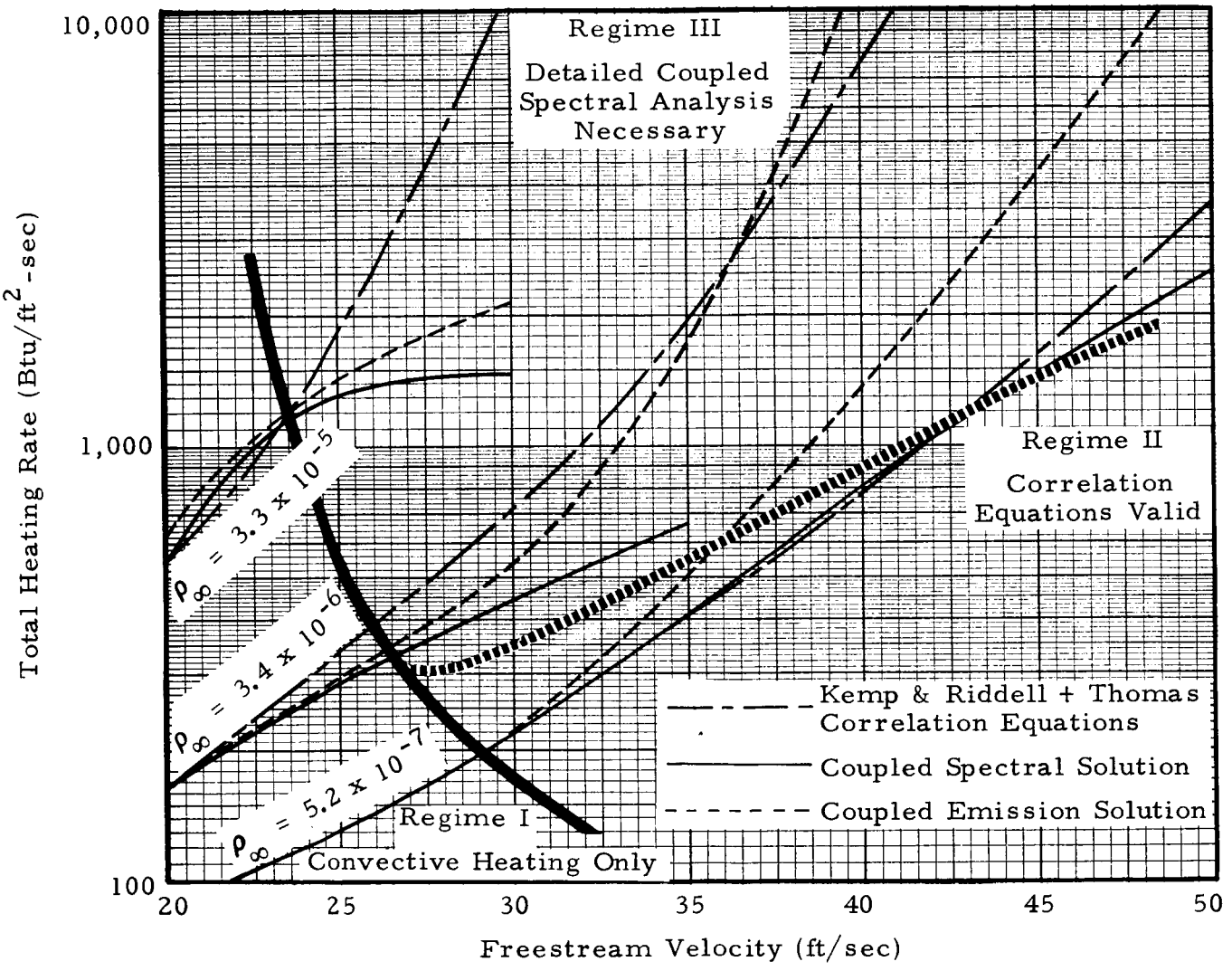

Figure 15 - A Comparison of Total Heating Rates Versus Freestream Velocity for Three Freestream Densities (R = 3 ft)

4.2 HEATING MINIMIZATION

Classically, an optimum body radius could be found that would minimize the total stagnation point heating rate at a particular trajectory point. This behavior is predicted by the addition of heating rates from convective and radiative heating correlation equations. Based on this concept, the optimum body radius that would yield the lowest total heating over a selected trajectory could be found by an iteration procedure. Further, a trajectory and a body radius could be selected to reduce total heating to a minimum by a calculus of variations procedure. A significant deviation from this classical concept due to radiation coupling has been presented by Dirling, Rigdon and Thomas (Reference 14). Their contention is that for many flight conditions the effects of radiation coupling changed the character of the heating rate versus body radius curve to the extent that no realistic minimum in heating rate occurs. The present study substantiates this conclusion.

Convective, radiative and total heating rates as a function of body radius are shown in Figure 16. A comparison between coupled heating rates computed using the detailed spectral and the emission model of this study are presented in Figure 16. Both methods yield results indicating that the total heating curve does not have a minimum. The spectral model yields coupled radiative heating rates which are substantially lower than those predicted using the emission model. Again, both models have the same type of variation with body radius. This indicates that the lack of a minimum is due principally to convective and radiation coupling rather than to the type of radiation model used.

Figure 16 also presents a comparison between heating rates predicted by the present analysis using the detailed spectral model and heating rates predicted by correlation equations of Kemp and Riddell and Thomas for various nose radii. The correlation equations predict the characteristic minimum in total heating due to the $1/\sqrt{R}$ dependence for convective and the R dependence for radiative heating. Solutions of the present study

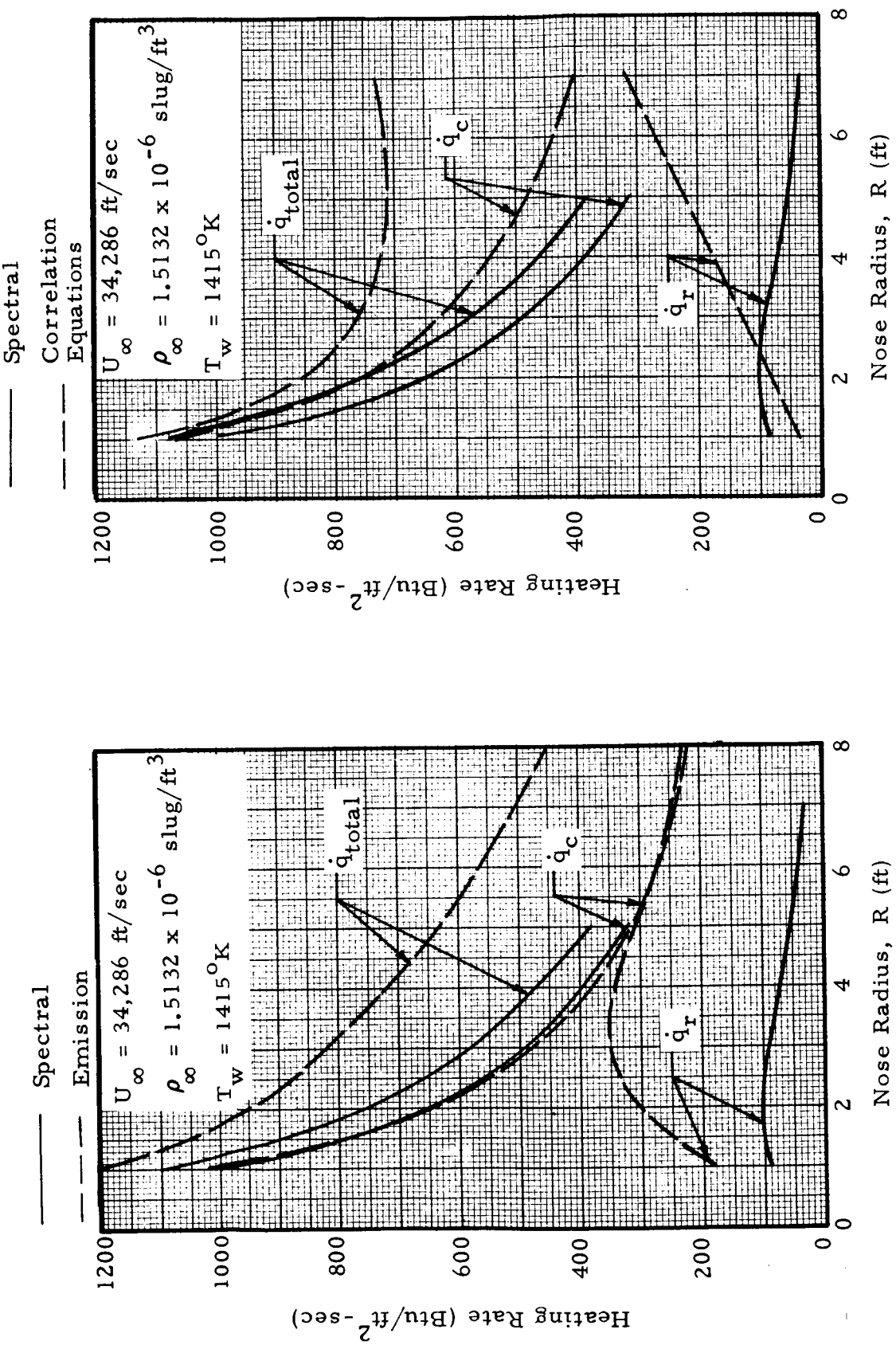

Figure 16 - Methods Comparison of Heating Rates as a Function of Body Radius

show that neither the $1/\sqrt{R}$ dependence for convective nor the R dependence for radiative heating holds for a coupled solution when a reasonable radiation model is used. In addition, at higher radii the value of the total heating is seriously overpredicted by adding equations for convective and radiative heating. The basic assumption in simply adding heating rates from equations for convective and radiative heating rates is that the convective and radiative heat transfer mechanisms are uncoupled. The extent of coupling increases with body radius. Therefore, in the event that coupling is small but exists at small radii, erroneous heating rates can be obtained from correlation equations at large radii because of the increased coupling.

4.3 MASS INJECTION EFFECTS

The injection of gaseous species into the shock layer changes the character of the layer and can significantly reduce the surface heating rate. To study mass injection effects with radiation coupling, a flight condition of U_∞ = 34,286 ft/sec and $\rho_\infty = 1.5132 \times 10^{-6}$ slug/ft^3 was selected. The effects of injecting various percentages of air at this flight condition where significant radiation coupling occurs are presented in Figures 17, 18 and 19 for a body radius of R = 3.066 ft. Injection of ablation products were not considered in this analysis, although this area is being explored for future analytical developments.

Since the intention of this portion of the analysis was to provide qualitative results for future quantitative studies, only the emission radiation model was used. Coupled heating rate solutions for mass injection rates, $(\rho V)_w$, up to 10% of the freestream mass flow rate, $(\rho U)_\infty$, are shown in Figure 17. The results presented in Figure 17 indicate that the total heating rate can be substantially decreased by mass injection. For the conditions analyzed, convective heating contributes very little to the total stagnation point heating for mass injection rates of approximately 5%. This behavior is clarified by Figure 18. The slope of the shock layer enthalpy profile at the wall is very near zero for large mass injection rates. Figure 18 also

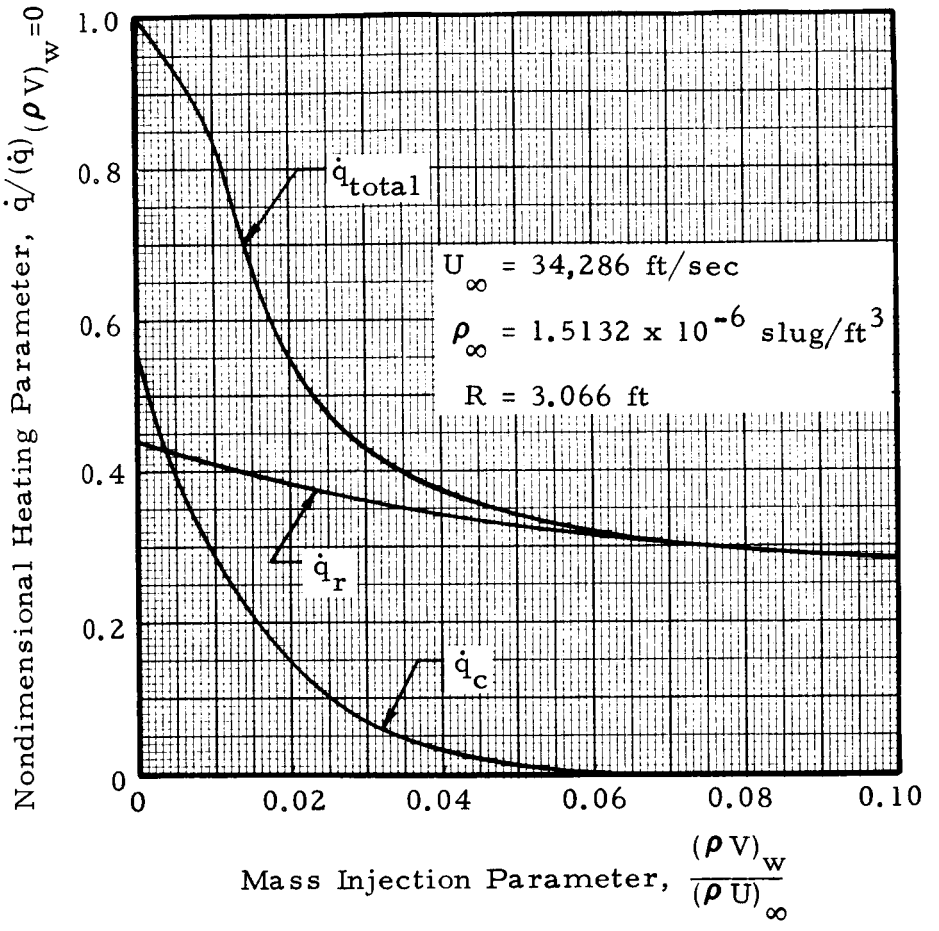

Figure 17 - Heating Rate Parameter Versus Mass Injection Parameter for a Coupled Emission Solution

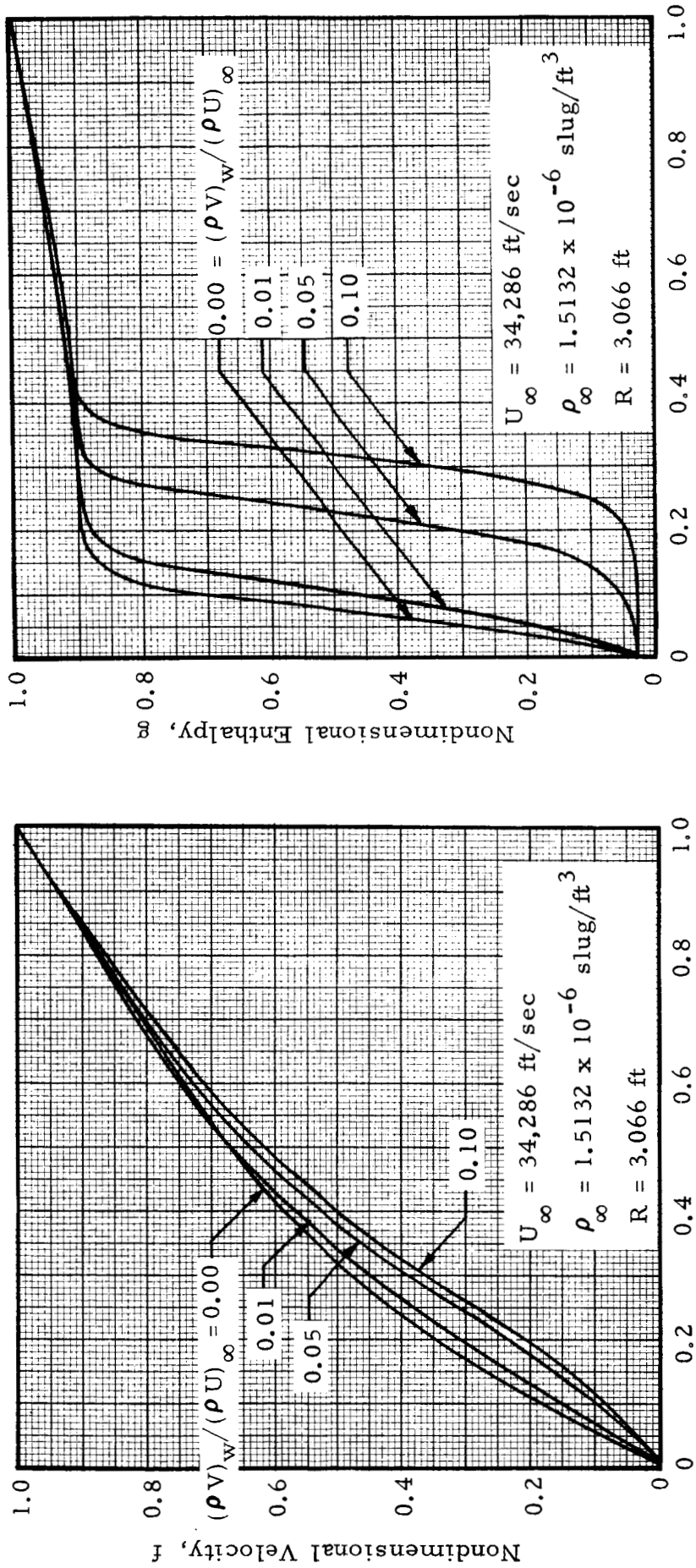

Figure 18 - Nondimensional Shock Layer Velocity and Enthalpy Profiles for Mass Injection Rates, $(\rho V)_w/(\rho U)_\infty$, of 0.0, 0.01, 0.05 and 0.10 (Coupled Emission Solutions)

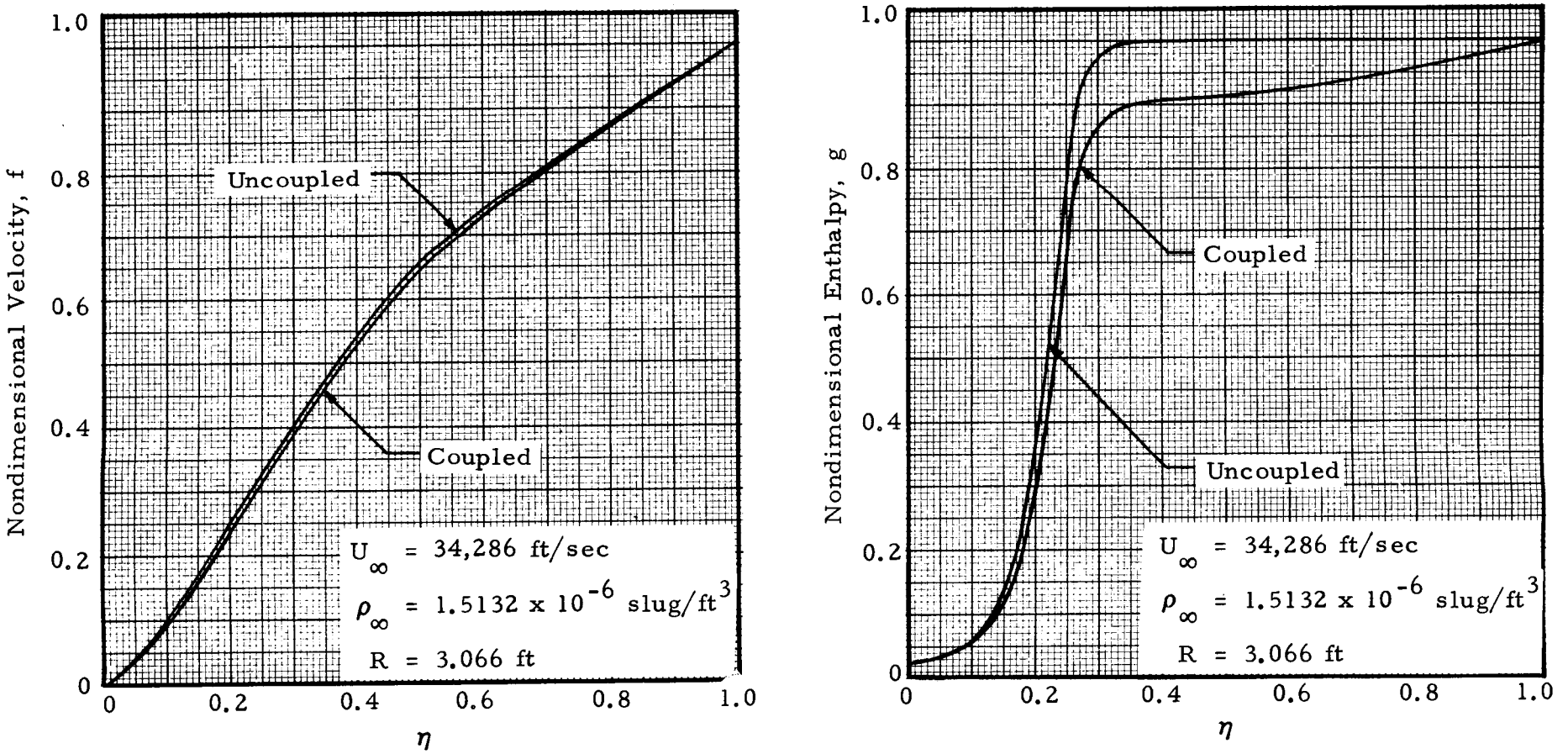

Figure 19 - Nondimensional Shock Layer Velocity and Enthalpy Profiles for Coupled and Uncoupled Emission Solution with a Nondimensional Mass Injection Rate of 0.05

shows that the shock layer velocity profile is affected by mass injection but not as significantly as the enthalpy profile.

The effects of convective and radiative coupling at a mass injection rate of 5% of the freestream value are shown in Figure 19. The shock layer velocity profile is only slightly reduced, while the enthalpy profile is appreciably reduced due to radiation cooling. It is interesting to note that the enthalpy profile near the wall and thus the convective heating is only slightly affected by convective and radiative coupling. Therefore, only the radiative heating, which dominates, is significantly affected by coupling for this high mass injection case. Furthermore, even for small mass injection rates, it can be concluded that a coupled solution is necessary for making realistic heating rate predictions when energy is transferred radiatively within a shock layer.

4.4 EARTH ENTRY AT LUNAR RETURN VELOCITIES

Reentry aerothermodynamics for reentry velocities above orbital velocities is complicated by strong coupling between radiative and convective heat transfer mechanisms. Coupling effects must be properly taken into account and realistic radiative properties must be used to determine adequately the heating environment on the blunted face of a reentry vehicle.

There are four principal areas in which the severity of the surface environment may be overpredicted and thus lead to unwanted or unexpected conservatism in a heat shield design. First, a realistic radiation model which properly accounts for self absorption must be used in order to predict realistic radiative heating rates. Secondly, and possibly more significantly, the radiative and convective heat transfer rates must be calculated using a coupled conservation equation solution. The effects of coupling on heating rates presented in previous sections demonstrates that highly conservative heating rates are obtained when this phenomenon is neglected. Neglecting the effects of mass injection on the heating rate is a third area in which conservatism can be introduced into a heat shield design. As seen

in Section 4.3 for injection of air species, a small amount of mass injection can significantly reduce the stagnation point heating rate, as well as change the character of the shock layer. A fourth area in which conservatism can be introduced is concerned with the degradation of ablation materials. In the present analysis, both coupling and mass injection are shown to decrease the velocity gradient at the wall (Figures 18 and 19). This, of course, decreases the shear stress at the wall and thus the degradation rate of an ablative surface. Also, as noted in previous sections, the extent of coupling increases with increasing body radius. Therefore, care must be exercised in using a shear stress analysis based on heating rate distributions from tunnel test on small nose radii model for design of a full-sized flight vehicle.

Figure 20 was prepared to illustrate the significance of the first two areas in which conservatism can be introduced into heat shield designs. This figure presents the stagnation point heating rate history for a 3.066 ft nose radius body using three theoretical methods. The heating rate curves are for the Project Fire II trajectory (Reference 14), which was used to simulate lunar reentry heating rates on the face of three beryllium calorimeters which were sequentially exposed. The three methods used were: (1) an uncoupled solution obtained by adding heating rates from correlation equations of Kemp and Riddell (Reference 13) and Thomas (Reference 13), (2) a coupled solution obtained using the analysis presented in previous sections for the emission model, and (3) a coupled solution obtained using the analysis presented in previous sections for the detailed spectral model. This figure shows that the heating rate is substantially reduced by coupling and self absorption in the portion of the trajectory where radiative transport of energy is significant. Further, the time at which peak heating occurs is changed by coupling.

In the light of the results presented here, it can be concluded that a detailed flowfield analysis is necessary for design of superorbital entry vehicle heat shields. All four major points where inadequately defined conservatism may be introduced into heat shield designs can be adequately defined using a detailed analysis. This is not beyond the state of the art at this time.

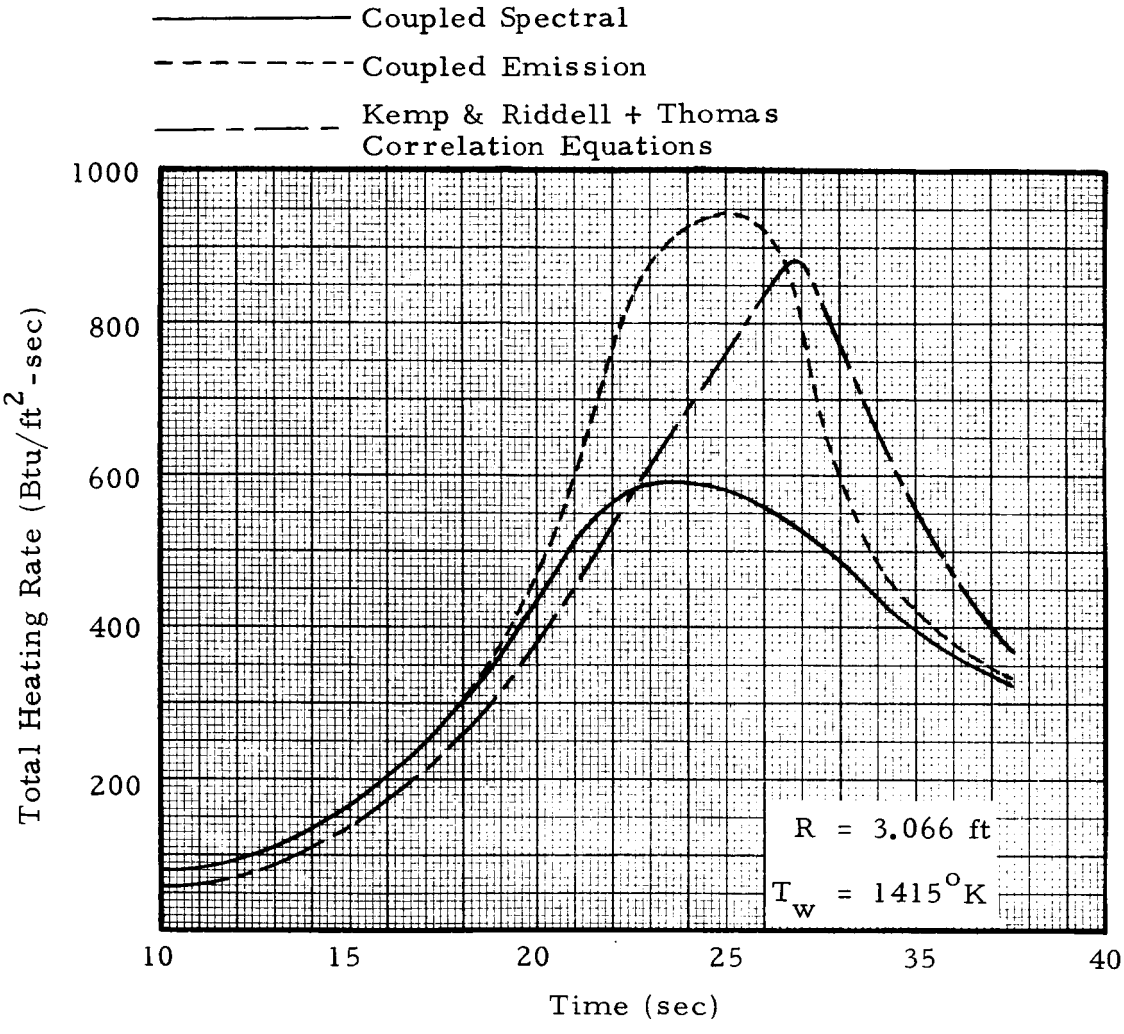

Figure 20 - Comparison of Heating Rates Predicted by Three Methods for Project Fire II Trajectory

REFERENCES

1. Spradley, L. W. and C. D. Engel, "Formulation of a Method for Predicting Coupled Convective and Radiative Heat Transfer about a Blunt Body," TM 54/20-165, LMSC/HREC A784881, Lockheed Missiles & Space Company, Huntsville, Ala., November 1967.

2. Hoshizaki, H. and K. H. Wilson, "Viscous, Radiating Shock Layer About a Blunt Body," AIAA J., Vol. 3, No. 9, September 1965, pp. 1614-1622.

3. Hoshizaki, H. and K. H. Wilson, "Convective and Radiative Heat Transfer During Superorbital Entry," AIAA J., Vol. 5, No. 1, 1967.

4. Spradley, L. W. and C. D. Engel, "A Computer Program for Predicting Coupled Convective and Radiative Heat Transfer to a Blunt Body During Superorbital Earth Entry," TM 54/20-191, LMSC/HREC A791350, Lock-Heed Missiles & Space Company, Huntsville, Ala., May 1968.

5. Hansen, C. F., "Approximations for the Thermodynamic Properties of High Temperature Air," NASA TR R-50, 1959.

6. Emmons, H. W. (Ed.), Fundamentals of Gas Dynamics, Vol. III, Ch. I, Tsien, H. S., "The Equations of Gas Dynamics," Princeton University Press, Princeton, New Jersey, 1958.

7. Scala, S. M., "The Equations of Motion in a Multicomponent Chemically Reacting Gas," Aerophysics Operation Research Memo No. 5, General Electric Company, Missile and Ordnance Systems Dept., Philadelphia, Pa., 1957.

8. Hoshizaki, H. and L. E. Lasher, "Convective and Radiative Heat Transfer to an Ablating Body," AIAA Thermo Physics Specialist Conference, Paper No. 67-327, 1967.

9. Maslen, S. H. and W. E. Moeckel, "Inviscid Hypersonic Flow Past Blunt Bodies," J. Aerospace Sci., 24, No. 9, 1957, pp. 683-693.

10. Blackledge, M. L. and C. J. Wojciechowski, "Real Gas Multiple Pressure Gradient Heating Rate Program," TM 54/20-114, LMSC/HREC A783781, Lockheed Missiles & Space Company, Huntsville, Ala., May 1967.

11. Browne, H. N., M. W. Williams and D. R. Cruise, "Theoretical Computation of Equilibrium Compositions, Thermodynamic Properties and Performance Characteristics of Propellant Systems," U. S. Naval Ordinance Test Station NAVWEPS, Report 7043, June 1960.

12. Yos, J. M., "Transport Properties of Nitrogen, Hydrogen Oxygen, and Air to 30,000°K," RAD-TM-63-7, March 1963.

13. Corning, G., Aerospace Vehicle Design, Brown-Brumfield, Inc., Ann Arbor, Mich., 1964.

14. Scallion, W. I. and J. H. Lewis, Jr., "Body Motions and Angles of Attack During Project Fire Flight II Reentry," NASA TN D-4183, October 1967.